

Overview of the QCD phase diagram - Recent progress from the lattice

Jana N. Guenther*

Aix Marseille Univ., Université de Toulon, CNRS, CPT, Marseille,
France

12/17/2020

In recent years there has been much progress on the investigation of the QCD phase diagram with lattice QCD simulations. In this review I focus on the developments in the last two years. Especially the addition of external influences or new parameter ranges yield an increasing number of interesting results. I discuss the progress for small, finite densities from both extrapolation based methods (Taylor expansion and analytic continuation for imaginary chemical potential) and Complex Langevin simulations, for heavy quark bound states (quarkonium), the dependence on the quark masses (Columbia plot) and the influence of a magnetic field. Many of these conditions are relevant for the understanding of both the QCD transition in the early universe and heavy ion collision experiments which are conducted for example at the LHC and RHIC.

1 Introduction

The strong interaction between quarks and gluons in the standard model is described by Quantum Chromo Dynamics (QCD). The investigation of the phase diagram of QCD has been an active subject for many years. A special focus of this research is on the transition between hadrons at low temperature and the quark gluon plasma at high temperature. The nature of the transition as an analytic crossover (Ref. [1–6]) has been known since 2006 (Ref. [1, 2]). However, different external influences may change the nature of this transition. One famous example is the addition of a chemical potential. The crossover has been established for vanishing baryon chemical potential only, which

*jana.gunther@univ-amu.fr

means for a setting with the same number of quarks and anti-quarks. This setting is a good approximation for the QCD transition in the early universe. However, the experimental investigations of the QCD transition rely on heavy ion collision experiments which produce the quark gluon plasma with a finite density. In addition, the collided matter goes through several stages and is not permanently in an equilibrium. Since, at the moment, full QCD cannot be solved under that conditions one has to take other paths. Certain parameter ranges can be described efficiently by effective theories. For other situations we depend on phenomenological models, which in turn require input information that can be gained from lattice simulations.

The progress on the phase diagram from lattice QCD corresponds well with, and is in part triggered by, an increasing number of available experimental results. At the moment most experimental results for heavy ion collision experiments are generated either by the Large Hadron Collider (LHC) at Cern in Genf, Switzerland or the Relativistic Heavy Ion Collider (RHIC) at the Brookhaven national laboratory in New York, USA. While the results from the LHC are at low densities, RHIC accesses information for larger chemical potential. However, there are several upcoming facilities that will allow access to even higher densities. Some of them are for example the Nuclotron-based Ion Collider fAcility (NICA) at the Joint Institute for Nuclear Research (JINR) in Dubna, Russia, the Compressed Baryonic Matter Experiment (CBM) at the Facility for Antiproton and Ion Research in Europe (FAIR) at Darmstadt, Germany and the J-PARC heavy ion project (J-PARC-HI) at the Japan Proton Accelerator Research Complex (J-PARC) in Tokai, Japan.

After this introduction, I will briefly describe the stages of a heavy ion collision experiment in section 2. Linking lattice QCD to heavy ion collision experiments requires results at low finite density which I discuss in section 3. The main challenge in this parameter range is the infamous sign problem which is discussed in section 3.1. For continuum extrapolated, physical results, one therefore has to rely on extrapolations (section 3.2) from vanishing (Taylor method) or imaginary chemical potential. One method that is getting relatively close to direct lattice simulations at finite density are Complex Langevin simulations, which are therefore reviewed in section 3.3. Other methods that are not discussed in this review are for example reweighting techniques [7–10], density of state methods [11, 12], using the canonical ensemble [13–15], formulations with dual variables [16] or Lefschetz thimbles [17, 18].

Another way to gain information on finite density QCD is discussed in section 4, the lattice simulations of effective field theories. Here, I focus, with section 4.1 on the results for heavy quark bound states the so called heavy quarkonium.

Despite the importance at finite density, also for zero density there are interesting influences to consider. One of them is the dependence of the transition type on the quark masses. It is often summarized in the Columbia plot, which is discussed in section 5. The most interesting areas of the Columbia plot are the upper right (section 5.5) and lower left corner (section 5.1). Due to the low quark masses, and the resulting expensive computations, different tactics are employed in the study of the lower left corner of the Columbia plot. In this review I discuss the use of imaginary chemical potential in section 5.2 and the variation of the number of quark flavors in section 5.3. Due to the lack

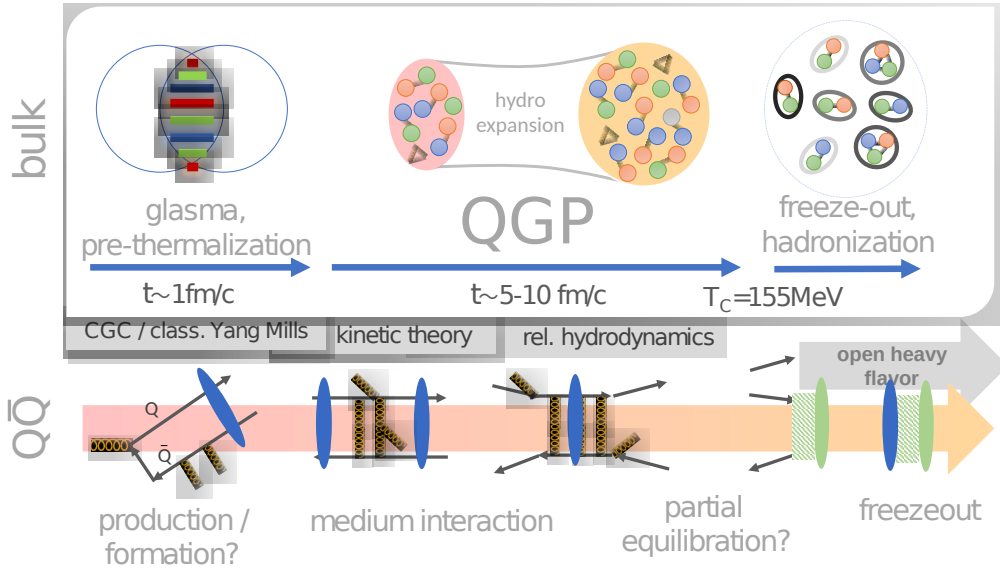


Figure 1: (Ref. [19]) Overview of the different stages of a heavy ion collision. In grey the different effective theories are shown which are used to describe the different stages (see section 4.1).

of continuum extrapolated results in this parameter range, I provide an overview over the numbers obtained from different lattice actions and lattice spacings in section 5.4.

There have been many results for yet another region. The addition of a magnetic field to finite temperature QCD does not suffer from a sign problem and is also relevant for the understanding of heavy ion collision experiments. The progress recently made on our understanding of the phenomena triggered by a magnetic field is discussed in section 6.

Finally, as common practice, this review closes with a conclusion. Here I hope to convince you that finite temperature lattice QCD and especially the investigation of the QCD phase diagram is a fascinating, thriving topic, of which I can only cover parts in this review.

2 Heavy ion collisions

As the experimental realization of QCD thermodynamics is strongly linked with heavy ion collision experiments, I will take a small detour to explain the different stages occurring during such a collision which are depicted in figure 1. In a heavy ion collision various nuclei can be used. Prominent examples are gold and lead which have been used at RHIC and LHC. Two beams of nuclei are accelerated to relativistic velocities.

When the two beams collide, they form a non thermalised state with strongly interacting fields, which is called a glasma and commonly treated in the color glass condensate framework (for details on this framework see Ref. [20, 21]). Here the glasma is seen in the infinite momentum framework where there are partons of the nuclei, valence quarks

and pairs of sea quarks. A main challenge is the description of different momentum scales. Due to the un-thermalised nature of this state, it is not accessible for lattice QCD simulations.

In the next stage, the further fragmentation of the partons into quarks and gluons leads to the quark gluon plasma. This is a strongly interacting state of deconfined quarks and gluons. While first it was expected to be similar to an electromagnetic plasma, by now it is well established that it is more similar to a strongly interacting fluid. Therefore, it is often described by relativistic hydrodynamics.

The quark gluon plasma expands and cools down at the same time. When it reaches temperatures close to the QCD transition temperature, the deconfined quarks and gluons have to recombine to colour-neutral hadrons. At this time, the chemical abundance of the hadrons is determined. The corresponding temperature is called the chemical freeze-out temperature. However, the hadrons can still exchange energy and momentum until the point where the kinetic freeze-out takes place.

An important question is, whether at the stage of the Quark-Gluon-plasma and the following transition to hadrons, the states thermalize. Only if this is the case, results from lattice QCD, which simulates thermal equilibrium, are directly applicable.

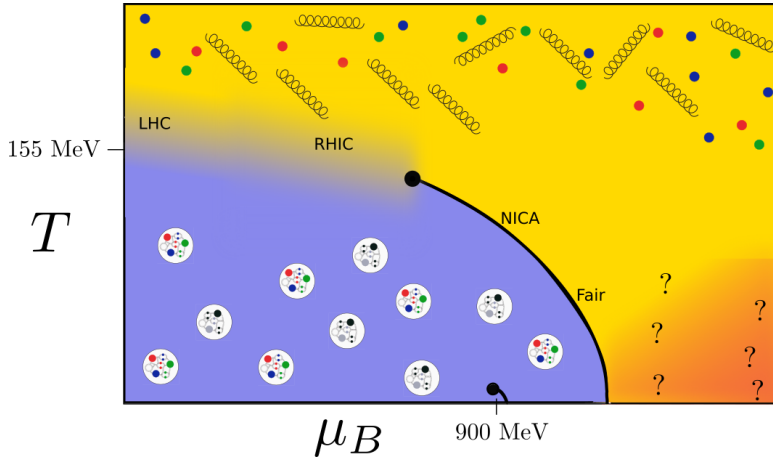


Figure 2: A schematic view on the T - μ_B -plane of the QCD phase diagram.

3 Low Finite density

One representation of the QCD phase diagram is in the T - μ_B -plane (figure 2). The $\mu_B = 0$ axis is well investigated by lattice QCD. For low chemical potential and temperature, there is a hadronic phase of colour neutral bound states. At high temperatures the effective degrees of freedom are the quarks and gluons. This phase is called the quark gluon plasma. These two phases are separated by a crossover at low and zero chemical potential. The transition is expected to change into a first order transition for higher μ_B with a critical second order point in between. The position of the critical point is under active investigation both by heavy ion collision experiments and by theoretic calculations. For very large chemical potentials further fascinating phenomena, like a colour super conducting phase [22], are expected.

To analyse the quark gluon plasma that is created in heavy ion collision experiments at the LHC or RHIC, a theoretical understanding of the quark gluon plasma in QCD is needed. In the region of the deconfinement transition, QCD can not be studied with perturbative methods. To get non-perturbative results with a controlled error, one has to turn to lattice QCD. At the moment, direct simulations that are continuum extrapolated and at physical quark masses are restricted to vanishing or imaginary chemical potential due to the infamous sign problem. On the other hand, the collisions especially at RHIC and upcoming heavy ion collision facilities like Fair and NICA take place away from the axis of zero μ_B . Therefore, information in that region are needed.

3.1 The sign problem

For simulation without chemical potential there are on average the same number of particles and antiparticles. Therefore, the expectation value of the overall baryon number density $\langle n_B \rangle$ is zero. To describe a system with finite baryon density, we need to introduce a finite quark chemical potential μ_q to the Lagrangian. In the continuum this is

relatively simple to achieve by adding a term of the form $\bar{\psi}\gamma_4\psi$. However, on the lattice, it is not that simple. Adding a similar term to the Dirac operator leads to a divergent energy density in the continuum limit, which is clearly unphysical. Instead one follows the idea of Hasenfratz and Karsch in [23] where the chemical potential is understood as the temporal component of a vector field. The temporal hopping term has then the form

$$\begin{aligned}
& - \frac{1}{2a} \sum_{n \in \Lambda} \left(e^{\frac{\mu}{T}} (\eta_4)_{\alpha\beta} U_{\hat{4}}(n)_{ab} \delta_{n+\hat{4},m} \right. \\
& \left. + e^{-\frac{\mu}{T}} (\eta_4)_{\alpha\beta} U_{\hat{4}}^\dagger(n-\hat{4})_{ab} \delta_{n-\hat{4},m} \right). \tag{1}
\end{aligned}$$

It recovers the original action for $\mu = 0$ and with $\frac{\mu}{T} = a\mu N_t$ it reproduces the correct density term at linear order in $a\mu$. However, this term breaks the γ_5 -hermiticity of the Dirac operator

$$\gamma_5 D \gamma_5 = D^\dagger \tag{2}$$

and leads to a complex fermion determinant for real μ . The fermion determinant enters in the Boltzmann weight factor which has to be positive to allow a Monte Carlo simulation. There have been several ideas on how to obtain results at real finite chemical potential like reweighting techniques [7–10], Taylor expansion [24–28], density of state methods [11, 12], using the canonical ensemble [13–15], formulations with dual variables [16], Lefschetz thimbles [17, 18] or complex Langevin [29, 30].

3.2 Extrapolation to finite μ

Instead of conducting direct simulations, for small densities it is possible to obtain results with physical quark masses by extrapolation. Since at $\mu_B = 0$ the transition is a crossover (Ref. [1–6]), certain observables can be parameterized by an analytic function in the vicinity of zero as well. This fact can be exploited, by using results at zero (Ref. [24–28, 31–39]) or imaginary chemical potential (Ref. [38, 40–53]), to find a function that can be extrapolated to real, positive chemical potential. If one aims at gaining information from zero chemical potential, one uses the higher order derivatives of the partition function to calculate the Taylor coefficients of an expansion that can be continued to finite μ_B . This method is therefore often called Taylor method.

The other possibility to determine a function that can be continued to finite chemical potential is the use of simulations at purely imaginary chemical potential, where there is no sign problem. As illustrated in figure 3, the data points can be described by a function of μ_B^2 . For imaginary chemical potential $\mu_B^2 < 0$ and this is the area where simulation results are available. The resulting data points can then be fitted with a function which can be extrapolated to $\mu_B > 0$ and therefore to real, positive chemical potential. Since not much knowledge of the concrete shape of the describing function is available, the choice of the fit function influences the result at real chemical potential.

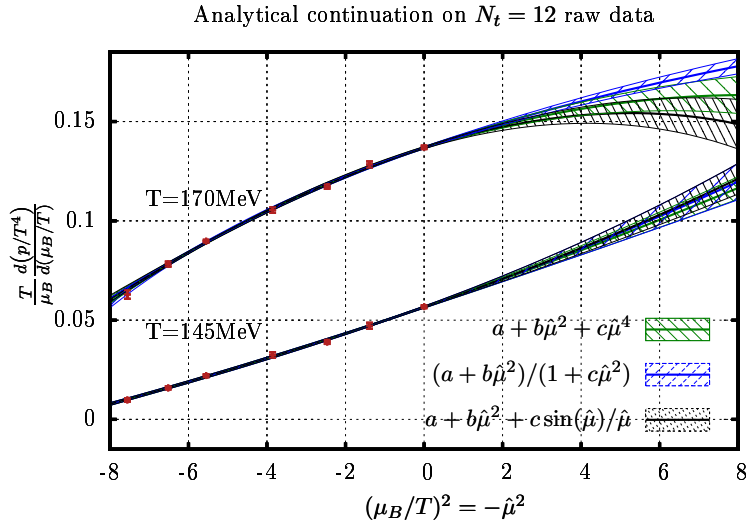


Figure 3: (Ref. [54]) Illustration of the analytic continuation from imaginary chemical potential. Data points generated with purely imaginary μ_B can be fitted as a function in μ_B^2 and then extrapolated from $\mu_B^2 \leq 0$ to $\mu_B > 0$.

Figure 3 shows three different fit functions, namely

$$f_1(\mu, T) = a + b \left(\frac{\mu}{T}\right)^2 + c \left(\frac{\mu}{T}\right)^4, \quad (3)$$

$$f_2(\mu, T) = \frac{a + b \left(\frac{\mu}{T}\right)^2}{1 + c \left(\frac{\mu}{T}\right)^2}, \quad (4)$$

$$f_3(\mu, T) = a + b \left(\frac{\mu}{T}\right)^2 + c \frac{\sin\left(\frac{\mu}{T}\right)}{\frac{\mu}{T}}, \quad (5)$$

which each having three fit parameters a , b , c . All three functions describe the available data well. However, their continuation to $\mu_B > 0$ varies, especially for a temperature of $T = 170$ MeV. This variation has, therefore, to be taken into account as a systematic error.

When utilising simulations at imaginary chemical potential, one exploits the fact that the γ_5 -hermicity of the Dirac operator with a chemical potential reads

$$\gamma_5 D(\mu) \gamma_5 = D^\dagger(-\mu). \quad (6)$$

This means that in the action, the term adding the chemical potential $e^{-\frac{\mu}{T}} = f$ is replaced by $(e^{\frac{\mu}{T}})^* = \frac{1}{f^*}$ when switching to purely imaginary μ . For the determinant this yields

$$\det(D(f)) = \det\left(D\left(\frac{1}{f^*}\right)\right), \quad (7)$$

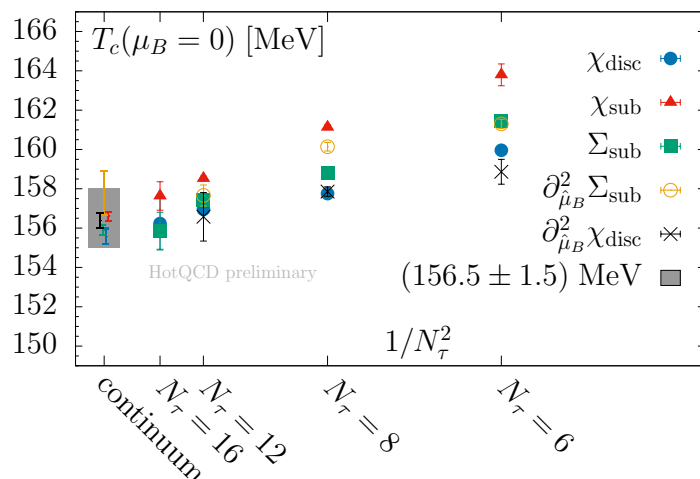


Figure 4: (Ref. [56]) The continuum extrapolation of five different definitions of the transition temperature. Towards the continuum limit the different definitions converge, yielding a combined result of $T_c = (156 \pm 1.5)$ MeV.

meaning that the determinant is only real if

$$f = \frac{1}{f^*}. \quad (8)$$

For real f this is only fulfilled if $f = e^{-\frac{\mu}{T}} = 1$, and, therefore, $\mu = 0$. However, if $\mu = i\mu^I$ is chosen to be purely imaginary, this yields

$$f = e^{-i\frac{\mu^I}{T}} = \left(e^{i\frac{\mu^I}{T}} \right)^* = \frac{1}{f^*}. \quad (9)$$

Thus the determinant is real for a purely imaginary chemical potential. When using simulations at imaginary chemical potential, less derivatives are needed than for the Taylor method. Instead, one uses different fit functions to describe a data set for several imaginary chemical potentials. This method is sometimes called analytical continuation, but, since also the Taylor method relies on an analytical continuation, I will refer to it as imaginary chemical potential method. The different fit functions can lead to different results which leads to the requirement of a careful systematic analysis. The behaviour of one type of fit functions, the Padé approximation, is discussed in Ref. [55].

The transition temperature: A common observable to extrapolate is the transition temperature. Because of the crossover nature of the transition, its definition is ambiguous. Typical definitions are, for example, the peak of the chiral susceptibility as a function of temperature or the inflection point of the chiral condensate. Often different definitions yield consistent results within the available precision. However for an analytic transition this is not guaranteed in contrast to the situation for phase transition.

A high precision determination of the transition temperature at $\mu_B = 0$ from five different observables was done in Ref. [56]. As can be seen in figure 4, all five definitions have the same continuum limit within the available precision. This yields a combined value of $T_c = (156 \pm 1.5)$ MeV.

A new definition as the peak of the chiral susceptibility as a function of the chiral condensate (instead of the more common definition as function of the temperature) was introduced this year in Ref. [53]. It allows for a precise extraction of the transition temperature and, therefore, also for an improvement in the extrapolation. The results obtained from simulations at imaginary chemical potential are shown in figure 5. They are continuum extrapolated from the three lattices with sizes $40^3 \times 10$, $48^3 \times 12$ and $64^3 \times 16$. The extrapolation was done with two different functions,

$$T_c = 1 + \hat{\mu}_B^2 \left(a + \frac{d}{N_t^2} \right) + \hat{\mu}_B^4 \left(b + \frac{e}{N_t^2} \right) + \hat{\mu}_B^6 \left(c + \frac{f}{N_t^2} \right) \quad (10)$$

and

$$T_c = \frac{1}{1 + \hat{\mu}_B^2 \left(a + \frac{d}{N_t^2} \right) + \hat{\mu}_B^4 \left(b + \frac{e}{N_t^2} \right) + \hat{\mu}_B^6 \left(c + \frac{f}{N_t^2} \right)}. \quad (11)$$

The transition temperature from imaginary chemical potential (*Analytical continuation* in the top of figure 5) is compared to the Taylor expansion at leading and next to leading order, as well as to results from truncated Dyson-Schwinger equations (Ref. [57]) and various determination of the chemical freeze-out temperature in heavy ion collision experiments (Ref. [58–62]).

The transition temperature at finite chemical potential $T_c(\mu_B)$ normalized by the transition temperature at zero chemical potential $T_c(0)$ is often parameterized by:

$$\frac{T_c(\mu_B)}{T_c(0)} = 1 - \kappa_2 \left(\frac{\mu_B}{T_c} \right)^2 - \kappa_4 \left(\frac{\mu_B}{T_c} \right)^4 + \mathcal{O}(\mu_B^6). \quad (12)$$

While there is a long history of the determination of κ_2 [28, 38–40, 46, 47], results for κ_4 [36, 53] only recently became available, both from the Taylor and imaginary potential method. It emerges that κ_4 is significantly smaller than κ_2 . Within its error it is still compatible with zero. A comparison of the recent determinations of both κ_2 and κ_4 is shown in figure 6.

Instead of an expansion in the baryon chemical potential, an expansion in isospin, strangeness or charge chemical potential is also an option. They were studied in detail in Ref. [36]. There are two very similar possibilities to chose μ_S and μ_Q for the expansion in μ_B that are commonly used. The first is the choice of a purely baryon chemical potential ($\mu_S = \mu_Q = 0$). This conditions have been used in Ref. [46]. The second possible choice is the set up at the strangeness neutral point. In this case μ_S and μ_Q are chosen in a way that $\langle n_S \rangle = 0$ and $0.4 \langle n_B \rangle = \langle n_Q \rangle$ to match the conditions in heavy ion collision experiments. This was done in Ref. [38, 47]. In all cases the two values agree within the error.

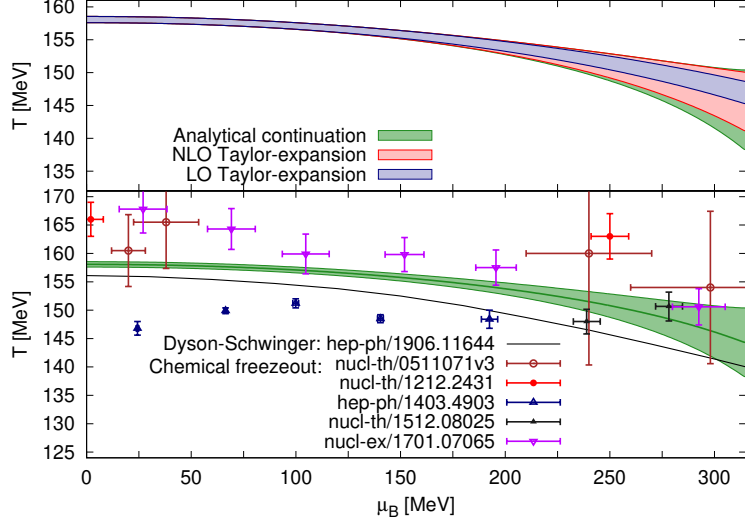


Figure 5: (Ref. [53]) Top: A comparison between the extrapolated transition temperature obtained from analytical continuation from imaginary chemical potential with different functions, compared to the result from extrapolating with the leading order (LO) order next to leading order (NLO) Taylor coefficients. Bottom: A comparison of the extrapolated transition temperature to recent results from calculations with Dyson-Schwinger-Equations [57] and the freeze-out temperature from heavy ion collision experiments [58–62].

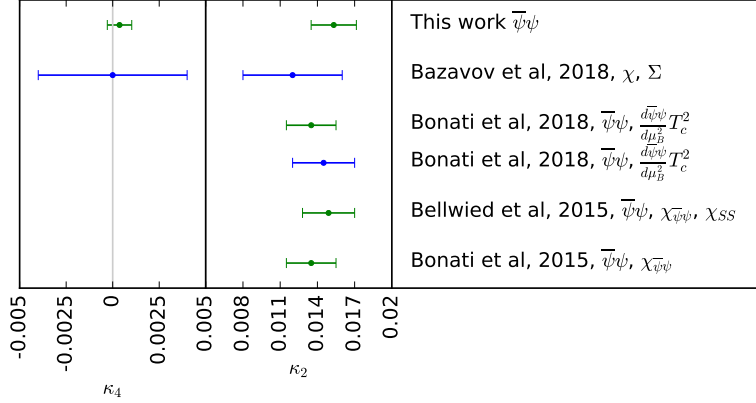


Figure 6: (Ref. [53]) A comparison of recent results for κ_2 and κ_4 as defined in equation (12). Ref. [36] and the lower point of Ref. [38] use the Taylor method and are depicted in blue. The green points, which are the result from Ref. [53], the upper point of Ref. [38], Ref. [47] and Ref. [46] used lattice data at imaginary chemical potential.

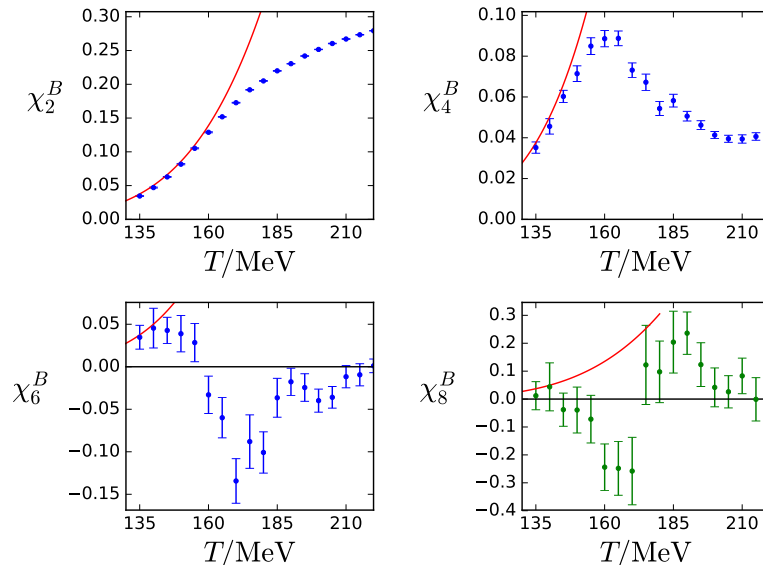


Figure 7: (Ref. [52]) Results for χ_2^B , χ_4^B , χ_6^B and an estimate for χ_8^B on a $N_t = 12$ lattice as functions of the temperature, obtained from the single-temperature analysis (see text). We plot χ_8^B in green to point out that its determination is guided by a prior, which is linked to χ_4^B . The red curve in each panel corresponds to the results from the Hadron Resonance Gas model.

Fluctuations: Higher order fluctuations of conserved charges are calculated as the partial derivatives of the pressure (or the QCD partition function) with respect to the chemical potentials. Here,

$$\chi_{i,j,k}^{B,Q,S} = \frac{\partial^{i+j+k}(p/T^4)}{(\partial\hat{\mu}_B)^i(\partial\hat{\mu}_Q)^j(\partial\hat{\mu}_S)^k} \quad (13)$$

with $\hat{\mu} = \frac{\mu}{T}$. These fluctuations are of great interest in the search for the critical endpoint, both for heavy ion experiments and theoretical calculations (Ref. [63–65]). They are proportional to powers of the correlation length and, therefore, expected to diverge in the vicinity of a critical end point (Ref. [26, 66–68]). Up to the 8th order fluctuations have been calculated on finite lattices in Ref. [31, 48, 52, 69]. The baryon fluctuations up to 8th order from Ref. [52] are shown in figure 7.

In principal, fluctuations can also be measured both on the lattice and experiments. A comparison between theoretical and experimental results can be used to extract the chemical freeze-out temperature T_f and the corresponding chemical potential μ_{Bf} as functions of the collision energy (Ref. [70–74]). To compare to experiments, one uses ratios of fluctuations to cancel out the explicit volume dependence. These can be matched to the ratios of cumulants of particle number distributions in experiments. However, not all baryons can be measured in experiments. Therefore, the cumulants of the proton

number distribution are considered a useful proxy to compare to the baryon number cumulants calculated on the lattice. Some combinations are:

$$R_{12}^B(T, \mu_B) = \frac{M_B}{\sigma_B^2} = \frac{\chi_1^B(T, \mu_B)}{\chi_2^B(T, \mu_B)} \quad (14)$$

$$R_{31}^B(T, \mu_B) = \frac{S_B \sigma_B^3}{M_B} = \frac{\chi_3^B(T, \mu_B)}{\chi_1^B(T, \mu_B)} \quad (15)$$

$$R_{42}^B(T, \mu_B) = \kappa_B \sigma_B^2 = \frac{\chi_4^B(T, \mu_B)}{\chi_2^B(T, \mu_B)} \quad (16)$$

$$R_{51}^B(T, \mu_B) = \frac{S_B^H \sigma_B^5}{M_B} = \frac{\chi_5^B(T, \mu_B)}{\chi_1^B(T, \mu_B)} \quad (17)$$

$$R_{62}^B(T, \mu_B) = \kappa_B^H \sigma_B^4 = \frac{\chi_6^B(T, \mu_B)}{\chi_2^B(T, \mu_B)}, \quad (18)$$

where the mean M_B , the variance σ_B^2 , the skewness S_B , the kurtosis κ_B , the hyper-skewness S_B^H and the hyper-kurtosis κ_B^H are the 1st to 6th order moments of the baryon number distribution.

New results on continuum estimates for R_{12}^B , $R_{31}^B(T, \mu_B)$ and $R_{42}^B(T, \mu_B)$ from lattice sizes $32^3 \times 8$ and $48^3 \times 12$ have been recently presented in Ref. [37]. For the comparison with experimental data along the transition line, $R_{31}^B(T, \mu_B)$ and $R_{42}^B(T, \mu_B)$ are shown (see top of figure 8) as a function of R_{12}^B . Therefore, it is not necessary to determine the temperature and chemical potential in a heavy ion collision separately. This allows for a comparison with data from the STAR collaboration (Ref. [75, 76]). The experimental datapoints fit the lattice results well.

First calculations of the 5th and 6th order cumulants from a $32^3 \times 8$ are presented in the same way at the bottom of Fig. 8. Here only preliminary experimental data (Ref. [76]) is available for a comparison with $R_{62}^B(T, \mu_B)$. While errors are still large, both on the lattice and the experimental side, there seems to be a tension between both data sets. Changing the lattice results such that they can describe the two available experimental points would require unexpectedly large higher order corrections.

In general, a detailed comparison between lattice data and experiment requires the incorporation of many different aspects (Ref. [60, 78–80]). While on the lattice side, clearly, a continuum extrapolation is still needed, on the experimental side it is not always clear which particle species allow for good comparisons to the conserved charges measured in lattice QCD. While for the cumulants for the baryon number distribution the proton number distribution has been established as reasonable proxy, for the strangeness number distribution the situation is less clear. A recent study in the hadron resonance gas (Ref. [77]) investigated different possibilities to find comparable observables. The comparison for different experimental proxies to the total, which would be the lattice result for $-\frac{\chi_{11}^{BS}}{\chi_2^S}$, is shown in Fig. 9. The lattice prediction for $-\frac{\chi_{11}^{BS}}{\chi_2^S}$ is calculated on an $48^3 \times 12$ lattice with two different methods. One that is based on the Taylor expansion and one that is based on the sector expansion (see Ref. [50]), where the pressure is

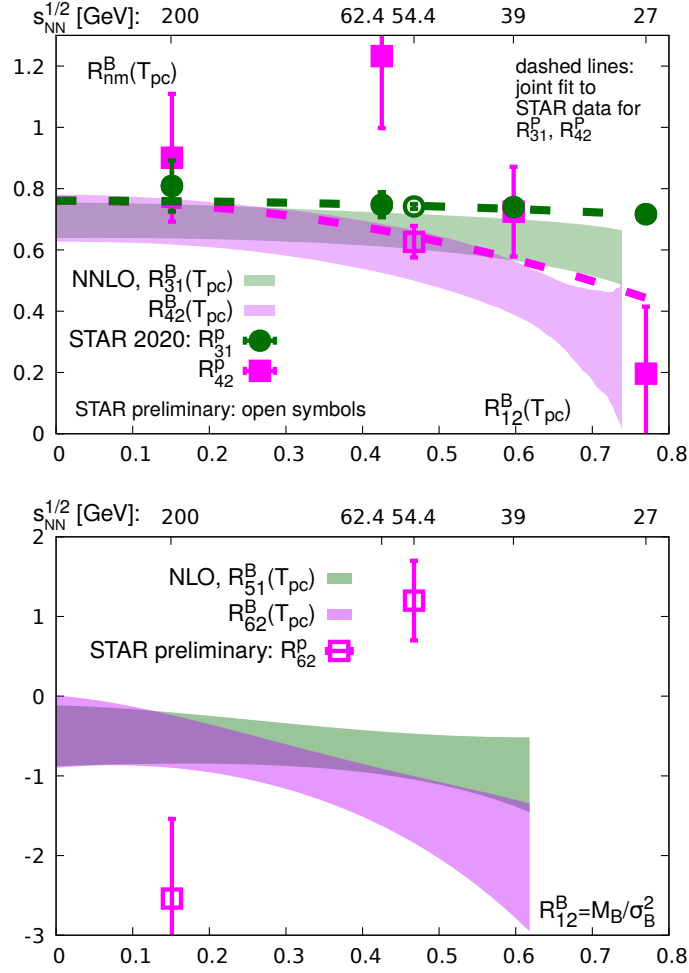


Figure 8: (Ref. [37]) Top: The ratios $R_{31}^B(T, \mu_B) = S_B \sigma_B^3 / M_B$ and $R_{42}^B(T, \mu_B) \equiv \kappa_B \sigma_B^2$ as a function of $R_{12}^B(T, \mu_B) = M_B / \sigma_B^2$ evaluated along the transition line in comparison to the data from the STAR collaboration (Ref. [75, 76]). The lattice calculation is a continuum estimate from $N_t = 8$ and $N_t = 12$ lattices. Bottom: The ratios $R_{51}^B(T, \mu_B)$ and $R_{62}^B(T, \mu_B)$ as a function of $R_{12}^B(T, \mu_B)$ evaluated along the pseudo-critical line in comparison to the data from the STAR collaboration (Ref. [76]). The lattice determination was done on an $N_t = 8$ lattice.

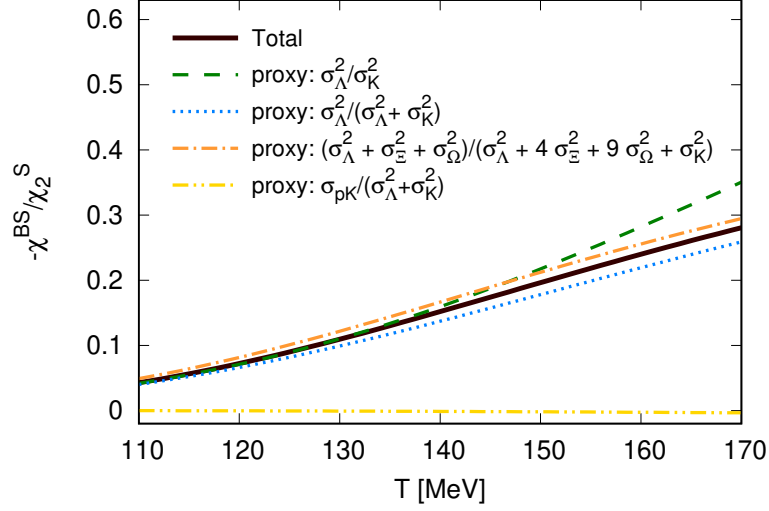


Figure 9: (Ref. [77]) Comparison between different possible combinations of particle number cumulants that could be measured experimentally (proxies) and the total of $-\frac{\chi_{11}^{BS}}{\chi_2^S}$ that could be determined in lattice QCD calculations. Both calculated in the Hadron Rasonance Gas model.

parameterized as

$$\begin{aligned}
P(\hat{\mu}_B, \hat{\mu}_S) &= P_{00}^{BS} + P_{10}^{BS} \cosh(\hat{\mu}_B) + P_{01}^{BS} \cosh(\hat{\mu}_S) \\
&+ P_{11}^{BS} \cosh(\hat{\mu}_B - \hat{\mu}_S) \\
&+ P_{12}^{BS} \cosh(\hat{\mu}_B - 2\hat{\mu}_S) \\
&+ P_{13}^{BS} \cosh(\hat{\mu}_B - 3\hat{\mu}_S) .
\end{aligned} \tag{19}$$

As can be seen in figure 10, both expansions agree well for small chemical potentials and temperatures around 140 MeV. For higher temperatures, a deviation between the two methods becomes visible before the errorbar grows due to the increased chemical potential. Also the influence of different experimental cuts has been investigated.

The critical endpoint: To look for a bound on the critical endpoint in the QCD phase diagram, one can try to calculate the radius of convergence of an expansion in μ_B around $\mu_B = 0$. When one wants to estimate the radius of convergence naively from the fluctuations, one defines

$$r_{2n}^\chi = \sqrt{\frac{\chi_{2n}}{\chi_{2n+2}}} . \tag{20}$$

If r_{2n}^χ converges, in the limit of $n \rightarrow \infty$, it is guaranteed that there is no criticality within this radius. This has been done in Ref. [35] for the fluctuations up to 6th order.

However, it has been shown in Ref. [81], that the ratio estimator as given in equation (20) is never convergent in a finite volume. This is consistent with the fact that

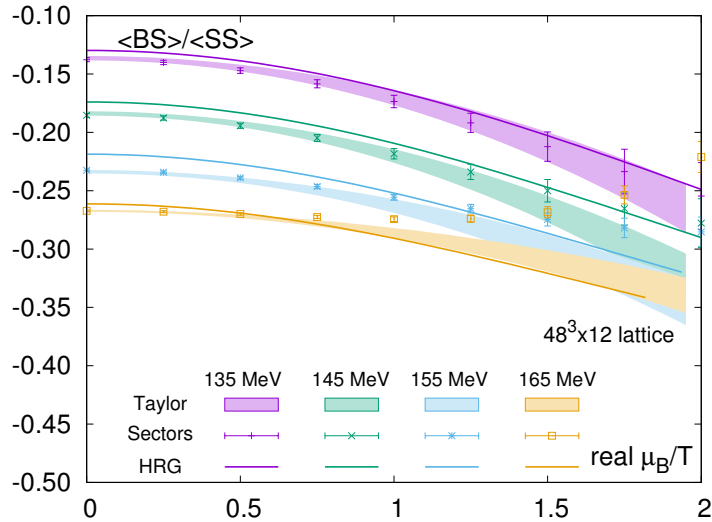


Figure 10: (Ref. [77]) Comparison between the Taylor and the sector method for $-\frac{\chi_{11}^{BS}}{\chi_2^{SS}}$ on an $48^3 \times 12$ lattice, as well as results from the hadron resonance gas model (HRG).

there is never a true phase transition in a finite volume. However, the convergence of the ratio estimator is problematic even when using the p_n extrapolated to infinite volume. It will work if one uses infinite-volume Taylor coefficients and the singularity determining the radius of convergence corresponds to a real phase transition in the infinite-volume limit. In the same work, alternative estimators have been discussed. Fig. 11 shows results on an $N_t = 4$ lattice for the standard estimator defined in equation (20), the modified Mercer-Roberts estimator

$$r_k^{(MMR)} = \left| \frac{(k+1)(k-1)c_{k+1}c_{k-1} - k^2c_k^2}{(k+2)kc_{k+2}c_k - (k+1)^2c_{k+1}^2} \right|^{\frac{1}{2}}, \quad (21)$$

and the doubled index estimator

$$r_k^{(2i)} = \left| \frac{2}{2kc_{2k} + k^2c_k^2} \right|^{\frac{1}{2k}}, \quad (22)$$

for a Taylor series with coefficients c_k .

Another way to look for a critical endpoint and find the radius of convergence is the investigation of the Lee-Yang zeros (Ref. [82]). These are the zeros of the partition function in the plane of complex chemical potential. The radius of convergence is the distance to the closest (leading) Lee-Yang zero in the infinite Volume limit. If this happens to be on the real axis, it is a signal for the critical endpoint. While the higher order fluctuations needed for a reliable radius of convergence estimate suffer from increasingly larger errors and are difficult to determine, Ref. [81] discusses a cancellation that allows

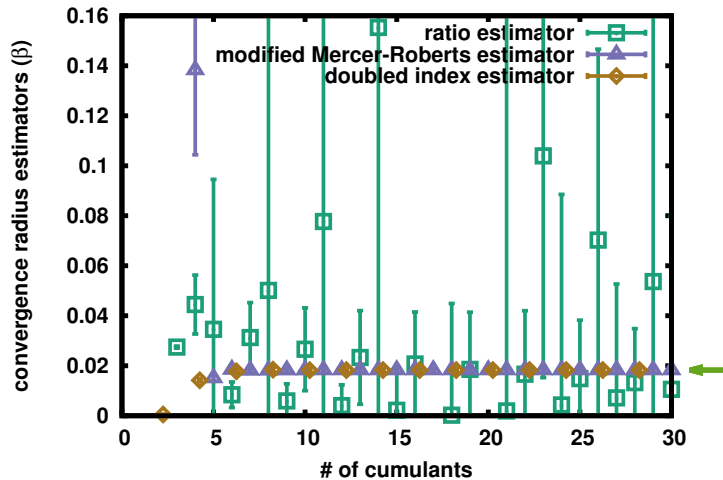


Figure 11: (Ref. [81]) The radius of convergence from three different estimators determined on an $N_t = 4$ lattice. The green arrow indicates the result from reweighting.

for a calculation of the leading Lee-Yang zero. However, this benefit only holds only if it is possible to reweight by using a reduced matrix formulation (Ref. [9, 83–86]). This is not possible for the case of rooted staggered fermions. For this case, Ref. [87] introduces a new definition of the rooted staggered determinant which allows for a numerical study of the Lee-Yang zeros. It is then tested on $N_t = 4$ lattice with stout smeared staggered fermions and a Symanzik improved gauge action. Spatial lattice extends of $N_s = 8, 10$ and 12 are used to estimate the infinite volume limit. However, this approach might still suffer from the overlap problem related with reweighting.

In Ref. [88], an algorithm called sign-reweighting is proposed, aiming to avoid uncontrolled systematics like the overlap problem. This approach separates the sign of the Dirac determinant $\det D(\mu)$ from the configuration generation which is done with a weight of $|\Re(\det D(\mu))|$. The sign is handled separately by a discrete reweighting.

3.3 Complex Langevin

One way to conduct lattice simulations, despite the sign problem that made significant progress are complex Langevin simulations. I will only give a very brief overview over the new developments. A more comprehensive recent review can be found in Ref. [89]. These simulations are based on the Langevin process, an evolution in a fictitious Langevin time, to generate configurations with a complex measure. This involves a complexification of all fields and, therefore, extending the $SU(3)$ gauge group to $SL(3, \mathbb{C})$, which is a non compact group. This can lead to so called runaway configurations which can cause the

trajectory to converge to a wrong result (Ref. [90–93]). To keep the evolution close to the unitary manifold and therefore to the correct result, gauge cooling (Ref. [29, 94]) was developed. A recent overview on this subject can be found in Ref. [95]. Even if the gauge cooling as well as an adaptive step size in the numerical integration (Ref. [96]) or the addition of force to the evolution [97] increase the stability of the Langevin simulations, it is still important to verify the correctness of the result. This can be done by different correctness criteria, which are related to the fall-off behavior of specific observables (Ref. [98–103]).

By now, results obtained with Complex Langevin simulations start to attacking the QCD phase diagram. In Ref. [104], Complex Langevin was combined with stout smearing and the result was compared with results from the Taylor expansion method (see section 3.2). The simulations were performed with four flavours of staggered quarks on $16^3 \times 8$ lattices with pion masses between 500 MeV and 700 MeV. The results for two different gauge actions, one unimproved and one with the Symanzik improvement, are shown in figure 12. The agreement between higher order Taylor and Complex Langevin results is good. These investigations were done at temperatures well above the transition temperature.

In Ref. [105], the transition is studied with two flavours of naive Wilson fermions and very heavy pion masses of about 1.3 GeV. The transition temperature is determined from the third order Binder cumulant

$$B_3(\mathcal{O}) = \frac{\langle \mathcal{O}^3 \rangle}{\langle \mathcal{O}^2 \rangle^{3/2}} \quad (23)$$

with two different Polyakov loop related observables \mathcal{O} . The data is then fitted with a quadratic function to determine the curvature of the transition line κ_2 (see equation 12). The transition line on an $N_s = 12$ lattice from both observables is shown in Fig. 13.

In addition to finite temperature studies, Complex Langevin simulations are also used to study low or zero temperature QCD. In Ref. [103, 106, 107], the average quark number $\langle N \rangle = N_f N_c N_s$ is studied on lattices with sizes $8^3 \times 16$ and $16^3 \times 32$. They found a plateau for $\langle N \rangle = 24$ as a function of the chemical potential. It is interpreted as the maximum number of zero momentum quarks that can exist at zero temperature. When the chemical potential is increased enough, it excites the lowest non-zero momentum states.

In Ref. [108], the zero temperature transition between hadronic and nuclear matter at a chemical potential of a third of the nucleon mass $\mu = \frac{m_N}{3}$ is searched for but not found. This contradiction to the physical expectation is related to possible issues with the Complex Langevin simulations, which faces difficulties at low or zero temperature.

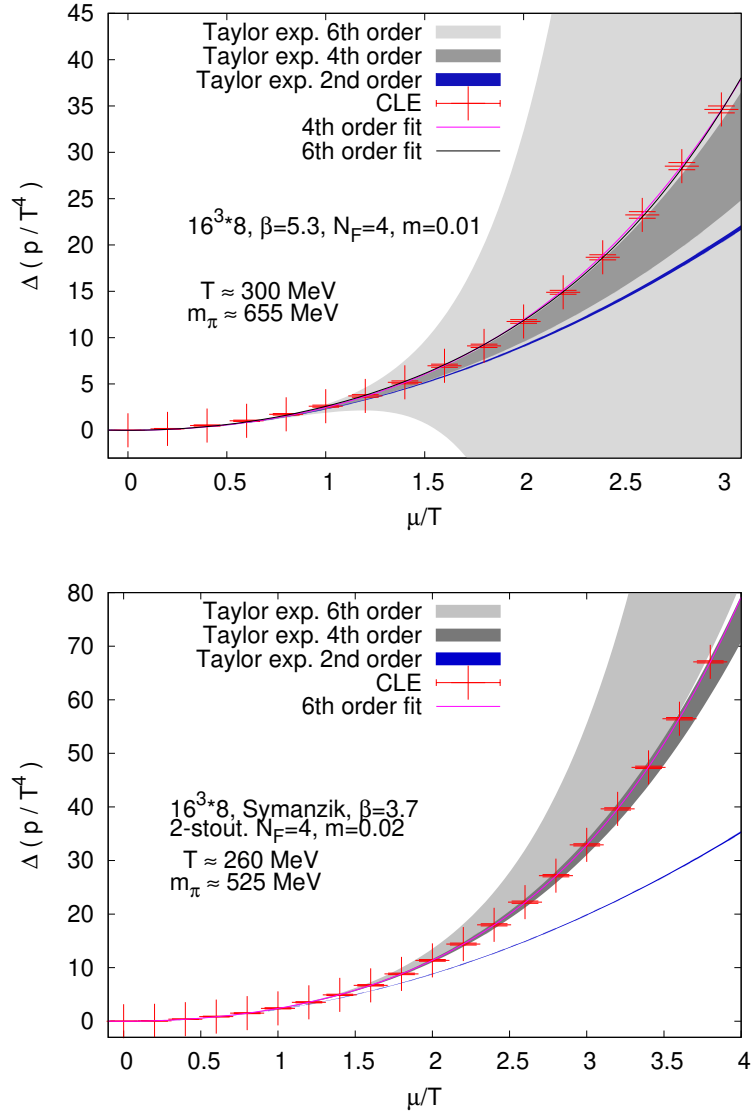


Figure 12: (Ref. [104]) Top: Comparison between an extrapolation by Taylor expansion (see sec. 3.2) and simulations with the complex Langevin equations using a naive action. Bottom: Comparison between an extrapolation by Taylor expansion and simulations with the complex Langevin equations using a Symanzik improved action.

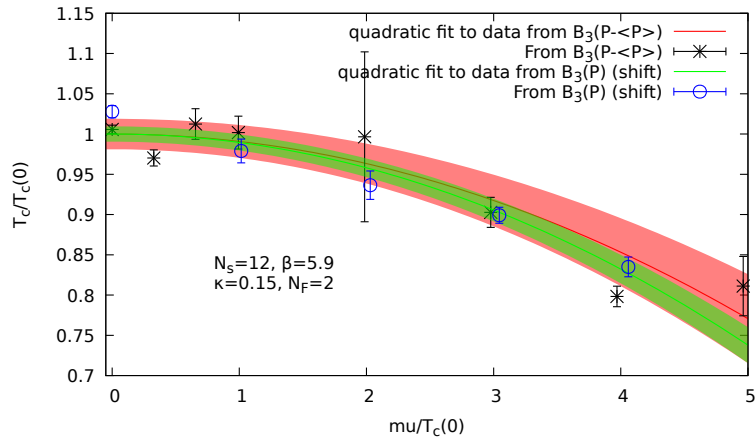


Figure 13: (Ref. [105]) The transition temperature from Complex Langevin Simulations at heavy pion masses ($m_\pi \approx 1.3$ GeV with two flavor Wilson fermions on an $N_s = 12$ lattice). The transition temperature is determined from the third order Binder cumulant B_3 with two different Polyakov loop related observables. The data is then fitted with a quadratic function.

4 Effective lattice theories

Full lattice QCD simulations for large baryon chemical potentials are out of reach for the moment. However, some insight can be gained from simulations of effective theories on the lattice. Here usually either the fermions and the spacial gauge links are integrated out, yielding a theory only depending on Polyakov loops, which contains the temporal link variables. Or, as the second common option, spatial and temporal gauge links are integrated out resulting in a theory with hadronic degrees of freedom. The use of effective theories is limited to a specific parameter range, where the reduction of the degrees of freedom holds true. If it is possible to find overlapping parameter ranges between different theories, one can gain insight in a wide range of phenomena.

4.1 Heavy Quarkonium

Heavy quarkonium refers to states of matter including heavy quarks, most commonly the charm and bottom quark. In heavy ion collisions, $c\bar{c}$ and $b\bar{b}$ pairs can usually only be created in early stages of the collision due to the required large energy amount. These heavy bound states are then surrounded by the quark gluon plasma and can either melt due to the high temperatures or survive until freezeout. In the later case, a signature for these particles should be visible in the detectors. Since the melting of different particles depends on the state of the quark gluon plasma, the observation of quarkonium is a useful tool to enhance our knowledge on QCD at very high temperatures. On the other hand it becomes more and more clear that not only the melting but also the possibility of recombination of quarkonium states has to be taken into account. The interaction between the heavy bound states and the surrounding medium is one of the main questions fueling the work on effective theories. A sketch of the different stages a heavy quark pair goes through in a heavy ion collision is shown at the bottom for figure 1 from Ref. [19] where detailed introduction and review of recent developments for heavy quarkonium can be found.

The input from the lattice to the investigation on quarkonium can be twofold. On one hand, the calculation of quarkonium correlators and their spectral functions as for example done in Ref. [109, 110]. Since these studies require zero temperature simulations, they are not part of this review.

On the other hand, the lattice simulations of effective field theories are a very helpful tool to investigate the behavior of quarkonium in a quark gluon plasma. To arrive at an effective field theory, the difference in scales within the quarkonium is exploited. The mass of a heavy quark m_Q is much larger than its velocity v within a bound state and, therefore,

$$m_Q \gg vm_Q \gg v^2 m_Q \quad (24)$$

as well as

$$m_Q \gg \Lambda_{\text{QCD}}. \quad (25)$$

The reduction of the degrees of freedom by the integration over different scales is sketched in figure 14. While full continuum QCD is valid at all scales, the finite volume of the

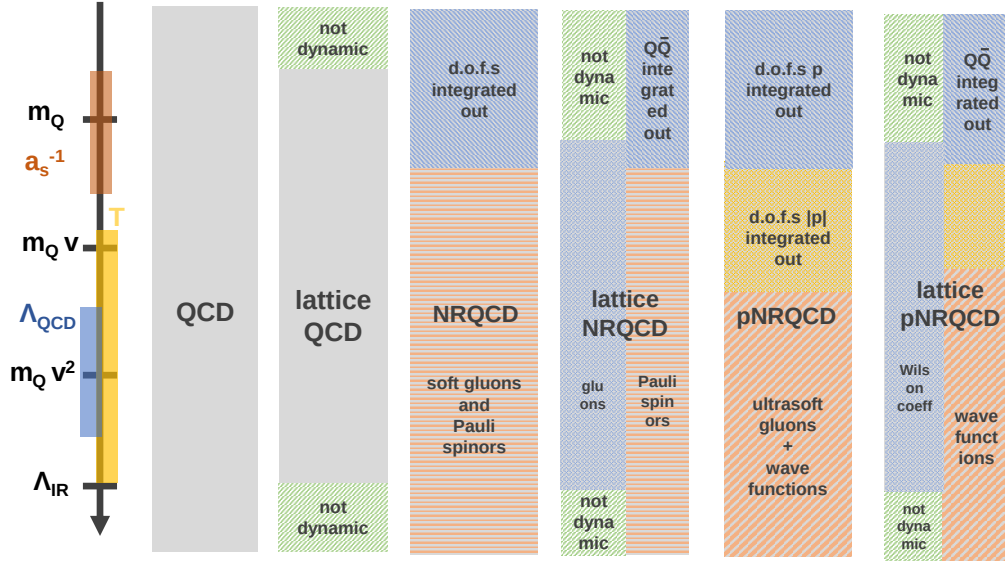


Figure 14: (Ref. [19]) Overview over the different scales treated in effective field theories on the lattice. In the first step the lattice introduces UV cut off by the finite lattice volume and an infrared cut off by the finite lattice spacing. In the next step gluons and heavy quarks are integrated out yielding a non relativistic version on QCD called NRQCD. The lattice version of NRQCD again has the respective cut offs. Instead of on the lattices NRQCD can also be treated perturbatively to integrated out further degrees of freedom down to an energy scale $m_Q v$. This leads to potential NRQCD (pNRQCD) with ultrasoft gluons and wavefunctions as remaining degrees of freedom. pNRQCD can then be studied on the lattice by the investigation of non-local Wilson coefficients.

lattice provides an infrared cut off, while the finite lattice spacing cuts off the ultraviolet divergences. To arrive at a non relativistic version of QCD called NRQCD (Ref. [111]) the hard gluons and heavy quarks are integrated out. The relevant degrees of freedom are the Pauli spinors and soft gluons. This effective theory itself can be treated by lattice simulation. On the other hand, a perturbative treatment of NRQCD can be applied to integrate out further degrees of freedom down to an energy scale $m_Q v$. This leads to potential NRQCD (pNRQCD, Ref. [112]), with ultrasoft gluons and wavefunctions as remaining degrees of freedom. In this framework the in-medium real-time potential can be investigated. Again, it is possible to study pNRQCD on the lattice. To construct the respective Lagrange functions for the various effective field theories, one identifies the relevant degrees of freedom at each energy scale and constructs a general Lagrange function from symmetry considerations. The relevant prefactors of each term, the so called Wilson coefficients, are determined by matching. The strength of effective field theories lies in the reduced number of degrees of freedom, that makes computations easier. The trade off is the reduced validity range.

An investigation of the validity of the perturbative treatment of effective field theory was done in Ref. [113]. There, lattice QCD calculations of a wide temperature range from 140 MeV up to temperatures of 5814 MeV with (2+1)-flavours of highly improved staggered fermions were performed. The evaluation of the static quark-antiquark potential led to the conclusion that effective field theories can be used between $0.3 \lesssim rT \lesssim 0.6$ (with r beginning the separation between quark and antiquark) to describe color screening reliably.

NRQCD: A large effort to use lattice NRQCD to study the behaviour of bottomonium in a quark gluon plasma has been undertaken by the FASTSTUM collaboration in Ref. [114–118]. They calculate the spectrum of bottomonium around the crossover temperature, using (2+1)-flavours of Wilson clover fermions on anisotropic lattices. The anisotropy of the lattices improves the NRQCD expansion. On the other hand it also leads to heavy pion masses of $m_\pi \approx 400$ MeV, if computation are to be kept affordable.

Another recent investigation of both bottomonium and charmonium using NRQCD has been done in Ref. [119, 120]. Here, lattice configuration of the HOTQCD collaboration with 2+1 highly improved staggered (HISQ) quarks were used. These ensembles have a realistic pion mass of $m_\pi \approx 161$ MeV. Ref. [120] was able to sort out previous tensions between Ref. [114] and Ref. [119] on the melting temperatures of quarkonium by relating them to different uncertainties in the spectral reconstruction. It was shown, that the mass of the ground state for heavy quarkonium reduces when the temperature is increased. However, in Ref. [121, 122], where the same configurations were analysed, the mass reduction was not observed.

pNRQCD: To investigate not only the ground state, but also the in-medium behaviour of excited quarkonium states, one has to turn to pNRQCD. Here the spectral functions are computed by solving the Schrödinger equation with a static potential. The results show a mass reduction for rising temperatures and agree well with lattice NRQCD results,

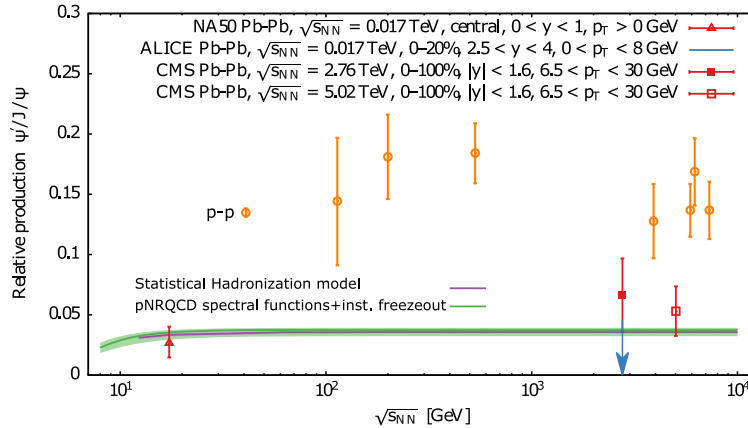


Figure 15: (Ref. [19, 123]) The ratio between ψ' and J/ψ from various heavy ion collision experiments: the NA50 (Ref. [124]), ALICE (Ref. [125]) and CMS (Ref. [126, 127]). The orange points show the pp baseline from Ref. [128, 129]. The purple line comes from the statistical model of hadronization from Ref. [128]. The green line is the result from a computation based on pNRQCD spectral functions combined with an instantaneous freeze-out scenario.

while contradicting expectation gained from perturbative pNRQCD.

Recent progress with computations in lattice pNRQCD include the determination of the ratio between the ψ' and J/ψ in Ref. [123]. Here a non perturbative treatment of pNRQCD is employed, based on the derivation of the generalized Gauss law. The derived potential is matched to lattice QCD results from Ref. [130–132]. The calculation of inmedium spectral functions allows for a prediction on the ψ' and J/ψ ratio, which is shown in figure 15. It is also compared to various results from heavy ion collision experiments as well as results from the statistical model of hadronization (Ref. [128]).

5 Columbia plot

As discussed before, for zero chemical potential and physical quark masses, the QCD transition is a crossover. However this changes when the quark masses are varied. The type of the transition between hadronic matter and the quark gluon plasma, called the QCD transition, depends on the quark masses. This is illustrated in the Columbia plot for 2+1 quark flavours (figure 16). The upper right corner, where quark masses are infinite, is the pure $SU(3)$ gauge limit with static quarks and exhibits a first order phase transition. Finite quark masses break the $Z(3)$ center symmetry of the zero mass limit explicitly, which weakens the phase transition until it becomes second order in the $Z(2)$ line bordering the upper right corner of the Columbia plot.

In the limit of vanishing quark masses, corresponding to the lower left corner of the Columbia plot, again a first order transition is expected for three flavours in the chiral limit, where $m = 0$. Finite quark masses break the chiral symmetry and weaken the transition until it becomes second order. This yields another $Z(2)$ line delimiting this corner. However, the case on the left border, for vanishing light quark masses, is still under investigation. Another possible scenario is that the first order region could extent all the way up to the $N_f = 2$ limit or hit the $m_{ud} = 0$ line at a finite strange quark mass, as shown in Fig. 16. The two scenarios are connected to the possible $U(1)_A$ symmetry reforestation at the transition temperature (Ref. [133, 134]) and are shown in figure 16.

The computation of the $Z(2)$ lines, especially in the lower left corner, are numerically very challenging. Smaller quark mass, as well as critical slowing down near a phase transition increase the computational cost. At the same time, small quark masses increase the taste breaking artifacts for the computationally relatively cheap staggered quarks, making a continuum extrapolation even more difficult. Also, scans in temperature, volume and quark masses are required to determine type and position of the transition. Due to this challenges, the only continuum extrapolated point in the Columbia plot up to now is the physical point (Ref. [1–6]).

To overcome the computational challenges faced when directly investigating the parameter space of the Columbia plot, additional extrapolation direction are used. Simulations at imaginary chemical potential can enlarge the first order region and help to determine it at $\mu_B = 0$ by limiting the search region. Similarly, simulations at variable N_f , even non integer ones, have been applied.

5.1 Lower left corner

One common direction of investigation is along the $N_f = 3$ diagonal of the Columbia plot. However, the first order region has only be found on $N_t = 4$ lattices with unimproved staggered (Ref. [135, 136]) or $O(a)$ -improved Wilson [137] fermions. For finer lattices or with further improved actions, the phase transition remains elusive (Ref. [138]).

A direct investigation along the $N_f = 2$ border only yielded results for $N_t = 4$ lattices with unimporved staggered or Wilson quarks (Ref. [44, 139, 140]).

A recent investigation of 2 + 1-flavor QCD with small quark masses is reported in Ref. [141]. It studies the the Polyakov loop expectation value $\langle P \rangle$ and the heavy quark

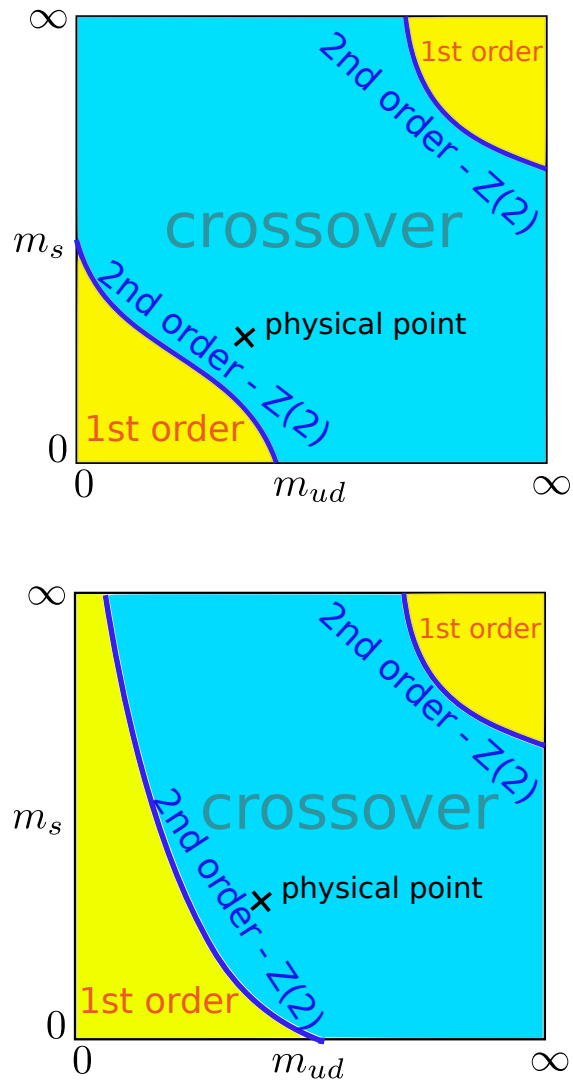


Figure 16: Schematic of two different, possible scenarios for the Columbia plot. It shows the dependence of the transition between hadronic matter and the quark gluon plasma on the quark masses.

free energy

$$F_q(T, H) = -T \ln \langle P \rangle = -\frac{T}{2} \lim_{|\vec{x}-\vec{y}| \rightarrow \infty} \ln \langle P_{\vec{x}} P_{\vec{y}}^\dagger \rangle \quad (26)$$

with $H = m_l/m_s$ on $N_t = 8$ lattices. The analysis is done for several volumes to reach the limit $H \rightarrow 0$. Result for the Polyakov loop and its derivative are shown in Fig. 17. It is found that the scaling behavior is consistent with the scaling behavior for energy-like observables in the 3-d, $O(N)$ universality classes. The authors observe a singular behavior of the quark mass derivatives of $\langle P \rangle$ and F_q/T . In the chiral limit the divergence is consistent with the 3-d, $O(2)$ universality class.

Previously, scaling studies have been carried out in Ref. [142, 143]. Here the transition temperature in the chiral limit T_c^0 and the magnetization

$$M = 2 \frac{m_s \langle \bar{\psi} \psi \rangle_l - m_l \langle \bar{\psi} \psi \rangle_s}{f_K^4} \quad (27)$$

as well as its derivative, the chiral susceptibility

$$\begin{aligned} \chi_M &= m_s (\partial_{m_u} + \partial_{m_d}) M |_{m_u=m_d} \\ &= m_s \frac{m_s \chi_l - 2 \langle \bar{\psi} \psi \rangle_s - 4 m_l \chi_{su}}{f_K^4} \end{aligned} \quad (28)$$

were determined from lattices with $N_t = 6, 8$ and 12 using the HISQ action. The pion mass was lowered down to $m_\pi \approx 55$ MeV and an $O(4)$ scaling ansatz was used to extrapolate to the chiral limit. The final result for the transition temperature in the chiral limit determined from different analyses is given as

$$T_c^0 = 132_{-6}^{+3} \text{ MeV}. \quad (29)$$

The dependence of the chiral susceptibility on the quark masses is shown in the top Fig. 18. It was determined on an $N_t = 8$ lattice. The spacial extent of the lattice is increased with decreasing light quark mass m_l . It is $N_s = 32$ for $\frac{1}{H} = \frac{m_s}{m_l} = 20$ or 27, $N_s = 40$ for $\frac{1}{H} = 40$ and $N_s = 56$ for $\frac{1}{H} = 80$ or 160. The dependence on the volume for fixed $\frac{1}{H} = 80$ is shown on the bottom for Fig. 18.

A further study on the chiral limit is done in Ref. [144]. Here again pion masses down to $\mu_\pi = 55$ MeV are used. Lattice spacing of $a = 0.12$ fm 0.08 fm and 0.06 fm corresponding to $N_t = 8, 10$ and 16. The authors investigate the dependence of the Dirac eigenvalue spectrum and the axial anomaly on the quark masses. For the chiral condensate they find that while there is a clear dependence on the quark masses and lattice spacing, the volume dependence is small. This is illustrated in Fig. 19.

Ref. [145] investigates the Columbia plot for the $N_f = 3$ case with improved Wilson quarks and the Iwasaki gauge action up to $N_t = 12$. It uses multiensemble reweighting to determine the minimum of the kurtosis. The change in this minimum as a function of β is then studied for different volumes. The point, where it agrees for several volumes defines the critical β value. A sketch of this so called kurtosis intersection analysis is shown in figure 20. The results for this analysis for five different values of N_t as well as

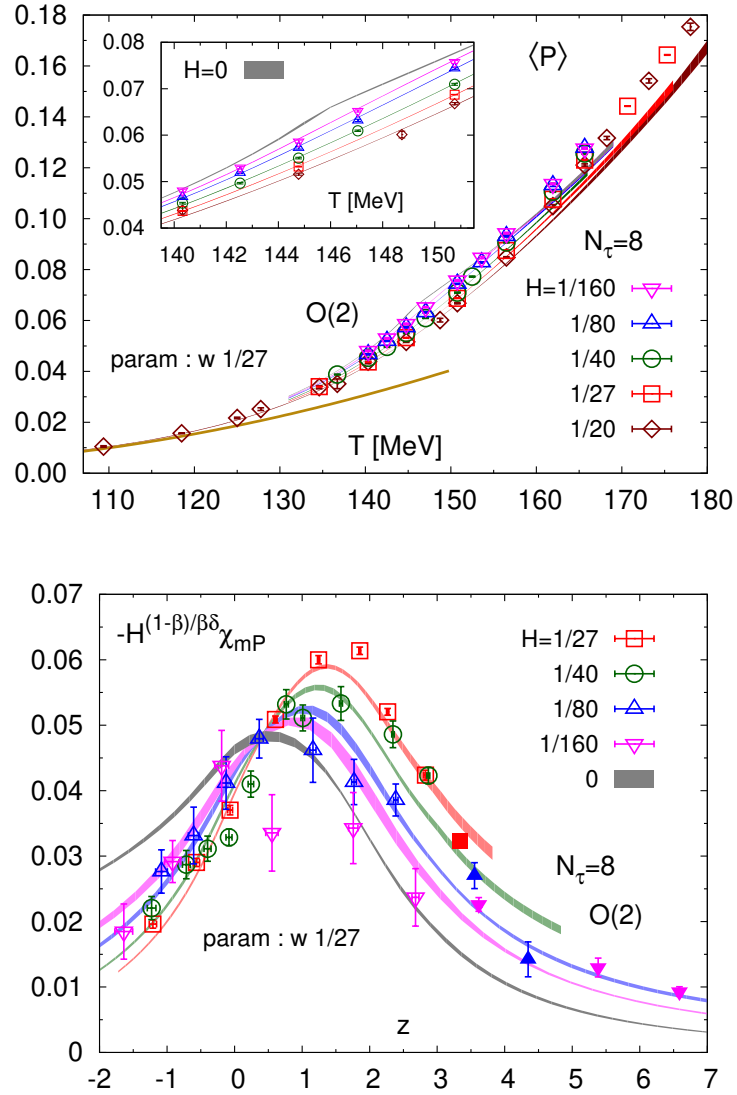


Figure 17: (Ref. [141]) Top: The temperature dependence of the Polyakov loop $\langle P \rangle$. Bottom: The derivative of the Polyakov loop as a function of the scaling variable $z = z_0 t H^{-1/\beta\delta}$ with $t = (T - T_c)/T_c$ and z_0, T_c being non-universal constants.

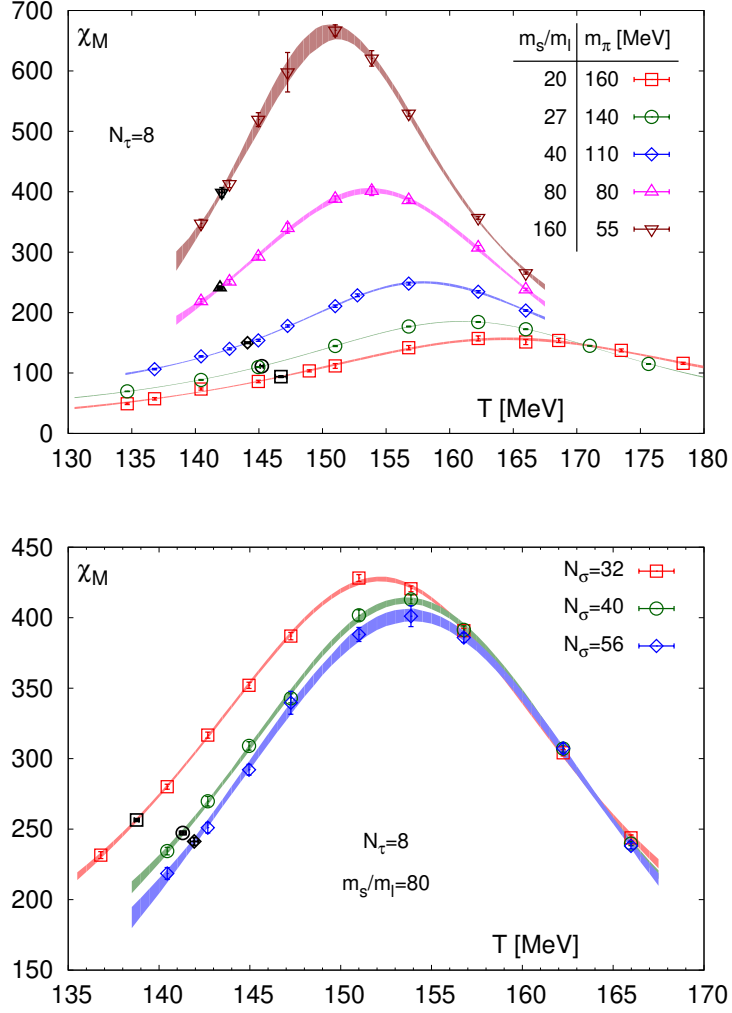


Figure 18: (Ref. [142]) Top: The quark mass dependence of the chiral susceptibility as defined in equation (28). Bottom: The volume dependence of the chiral susceptibility as defined in equation (28).

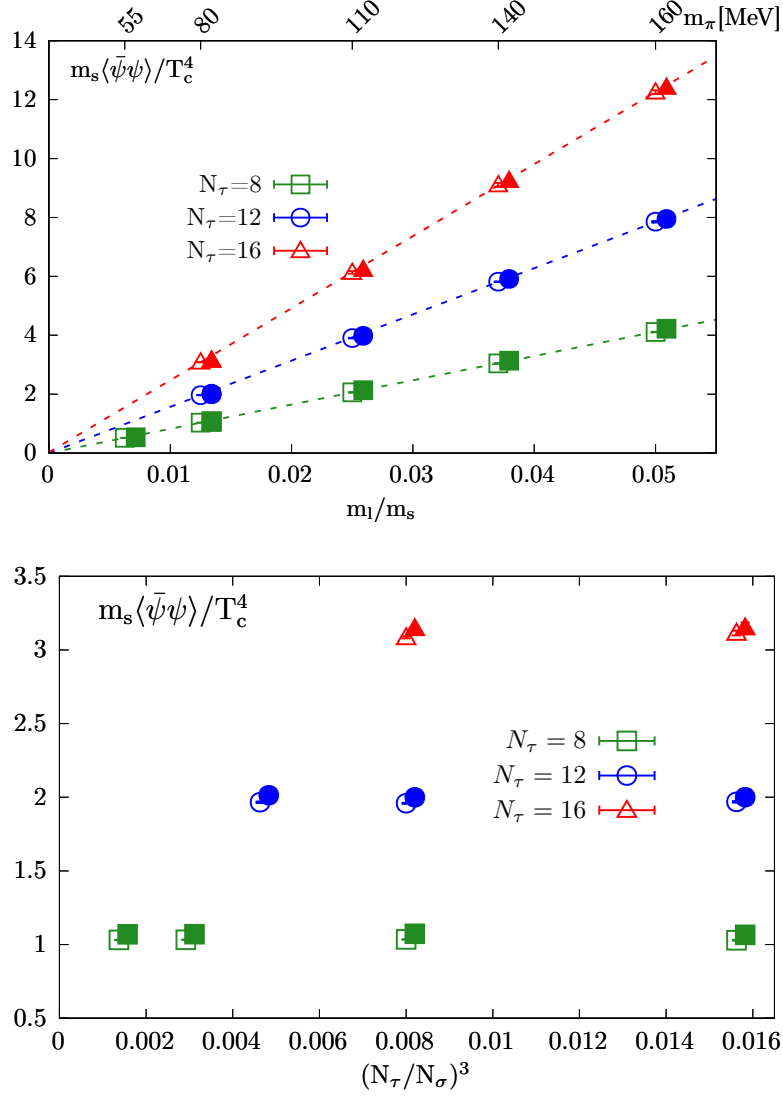


Figure 19: (Ref.[144]) Top: The quark mass dependence of the chiral condensate for different lattice spacing. Bottom: The volume dependence of the chiral condensate for different lattice spacings at $m_\pi = 80$ MeV.

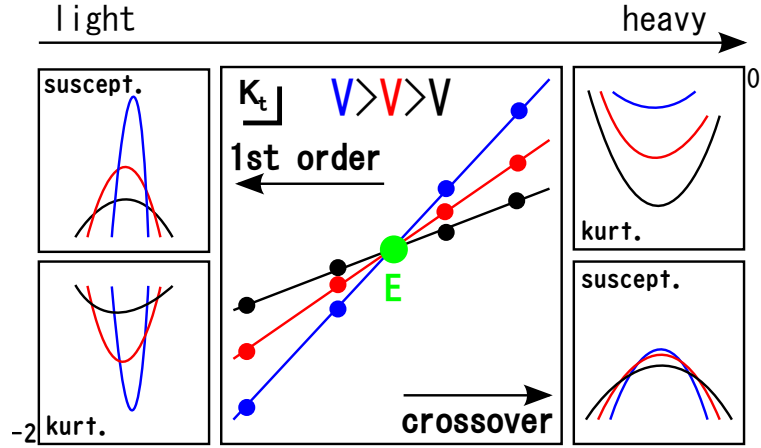


Figure 20: (Ref. [145]) Sketch of the kurtosis intersection analysis. The minimum of the kurtosis is determined from multiensemble reweighting and the then fitted for different volumes. The intersection is taken to be the value for the critical endpoint, as here there should be no volume scaling.

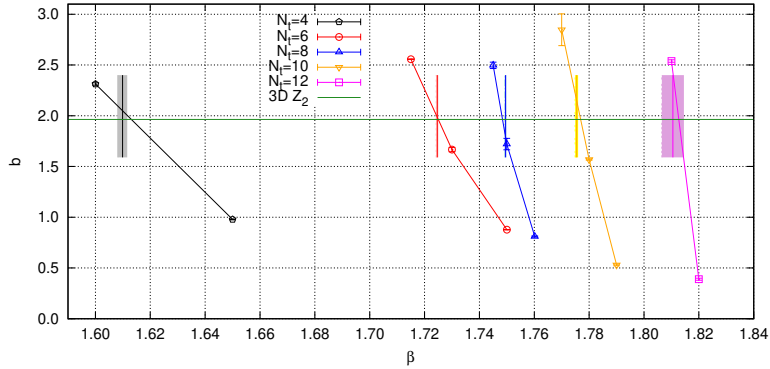


Figure 21: (Ref. [145]) The scaling exponent of the maximum susceptibility with the volume: $\chi_{\max} \propto (N_s)^b$. The results are shown for $N_t = 4, 6, 8, 10$ and 12 with connecting lines. The green horizontal line shows the expectation for $Z(2)$ -scaling. The shaded areas show the results for the critical β from the kurtosis intersection analysis.

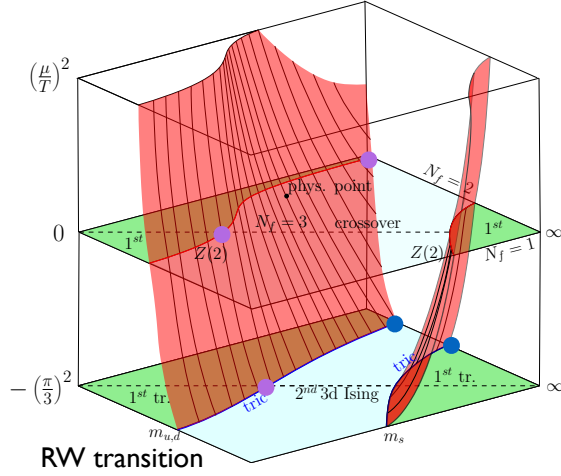


Figure 22: (Ref. [133]) Sketch of the 3d-Columbia plot with added chemical potential.

the scaling of the maximal chiral susceptibility $\chi_{\max} \propto (N_s)^b$ is shown in figure 21. The authors conclude that the $Z(2)$ line in the Columbia plot for the $N_f = 3$ case (along the diagonal) is located at a pion mass $m_\pi \lesssim 110$ MeV.

5.2 Imaginary chemical potential

One way to enlarge the first order region of the Columbia plot, at least on coarse lattices, is the introduction of an imaginary chemical potential. As discussed in section 3.2 there is no sign problem in QCD the case of an purely imaginary chemical potential. A sketch of this 3d-Columbia plot is shown in Fig. 22. When adding the chemical potential axis to the Columbia plot, its curvature at $\mu = 0$ is negative. This increases, therefore, the first order region for imaginary chemical potential and decreases it for real μ . This investigations have been done both with unimproved Wilson (Ref. [146]) and staggered (Ref. [147, 148]) fermions on $N_t = 4$ lattices.

5.3 Variable N_f

Another way to increase the strength of the phase transition, and therefore helping with the investigation of the Columbia plot, is to increase the number of flavours N_f . Ref. [149] studies the Columbia plot with four staggered quarks and the Wilson plaquette action. The choice of $N_f = 4$ has the added benefit that no rooting is required. Simulations were performed for $N_t = 4, 6, 8$ and 10 for several spacial lattice extends. Figure 23 shows the difference between the critical pion mass for four or three staggered quarks. The increased number of flavours increases the pion mass, so that simulations on lattices with larger temporal extend are possible.

To get a smooth transition between the integer number of flavours, it is even possible

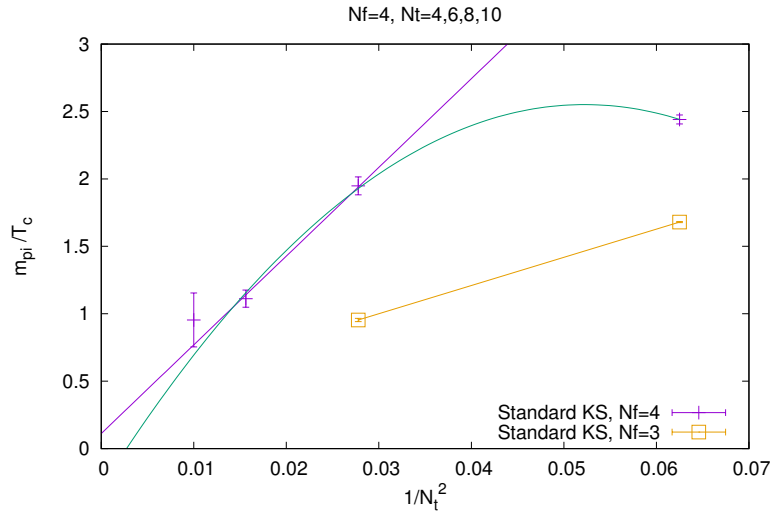


Figure 23: (Ref. [149]) The value of the critical pion mass for four or three staggered quarks, for different values of N_t . For four flavours the critical mass is larger, allowing to to to finer lattices.

to consider non-integer powers of the quark determinant (Ref. [139]). This allows for a smooth interpolation in N_f . Since in the ciral limit the transition is second order for $N_f = 2$ and first order for $N_f = 3$ there has to be a tricritical scaling area, with a critical point at N_f^{tric} , in between. Ref. [139] presents results on $N_t = 4$ lattices for $N_f = 2.8, 2.6, 2.4, 2.2$ and 2.1 . The dependence of the critical mass m_{Z_2} for a $Z(2)$ scaling is expected to follow

$$m_{Z_2}^{2/5}(N_f) = C (N_f - N_f^{\text{tric}}). \quad (30)$$

The result are shown in the top of figure 24. The rescaled mass is shown in the bottom of figure 24. A linear function was fitted to the rescaled mass to determine C and N_f^{tric} .

5.4 Overview - lower left corner

The investigation of the Columbia plot remains a challenge for lattice QCD. For the determination of the second order line in the lower left corner (see figure 16) several results are available on finite lattices however there is no clear solution for the continuum limit. Figure 25 shows an overview over the results for different fermion types. For this plot, some conversions were necessary. Some values were converted to MeV using the value for the critical temperature from Ref. [150] $T_c = (156 \pm 8)$ MeV for coarse lattices and staggered quarks. Upper bounds are denoted by zero with the errorbar showing the bound. Values given without any error, are assumed to have 50% relative error. The color of the points denotes the fermion type used in the simulations. Red stands for unimproved staggered, orange for improved staggered, green for unimproved Wilson and blue for improved Wilson quarks. The largest number of results is available for the three

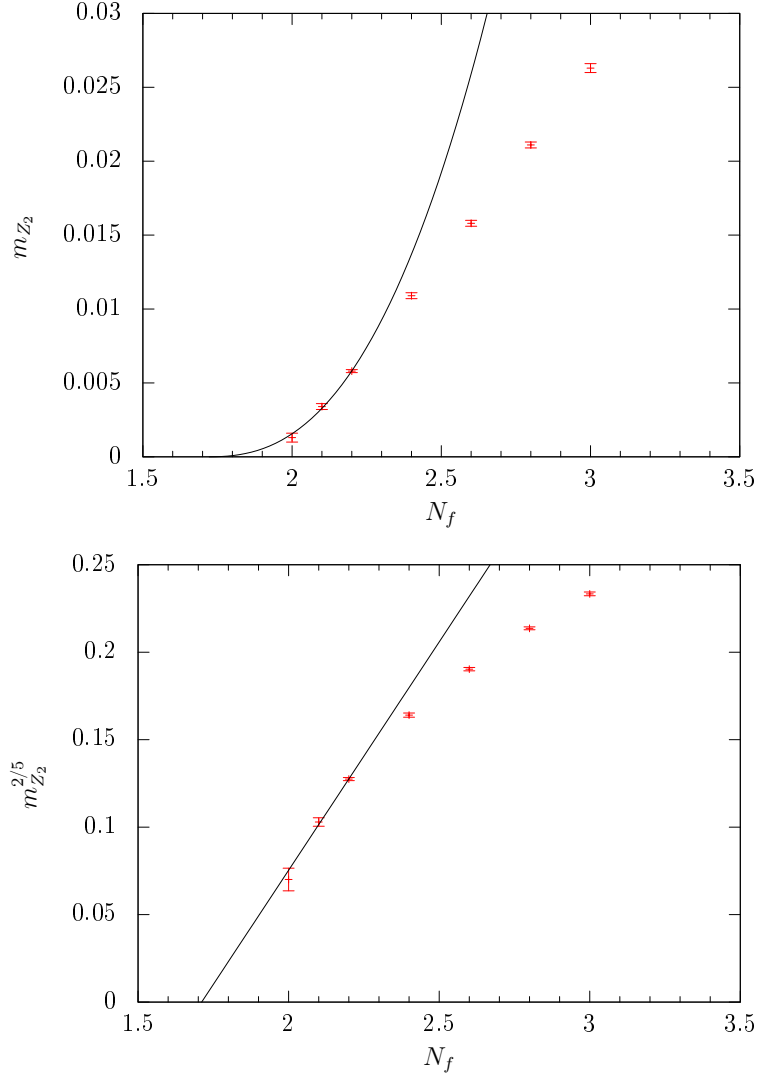


Figure 24: (Ref. [139]) Top: The critical mass m_{Z_2} as a function of the number of flavour. The black line is the rescaled version of the fit done to the rescaled mass below. Bottom: The rescaled critical mass m_{Z_2} as a function of the number of flavour. As well as a linear fit to the data.

flavour case. Here both Wilson and staggered quarks show a shrinking value when the lattices become finer. The same trend can be observed for staggered quarks with $N_f = 4$. For both two and three flavors, staggered quarks show smaller values than Wilson quarks. Also for staggered quarks an improvement of the quark formulation reduces the value for the critical pion mass. Assuming that all quark formulations agree in the continuum, which they should, it seems that still a large amount of computational power is needed to settle the shape of the lower left corner of the Columbia plot. Investigating this region becomes especially challenging since both staggered and Wilson quarks suffer from large lattice artifacts when the quark masses become small (Ref. [151]).

5.5 Upper right corner

Recent progress on the determination of the upper right corner of the Columbia plot (see figure 16) was reported in Ref. [157]. The authors determine the critical pion mass for the $N_f = 2$ flavour case. This corresponds to the upper border of the Columbia plot. The lattice setup consisted of two dynamical, degenerate Wilson fermions on lattices with $N_t = 6, 8$ and 10 . These N_t values correspond to lattice spacings between 0.07 fm and 0.12 fm. The results for the critical pion masses m_π^c for all three lattices are shown in the bottom of figure 26. While a precise continuum limit is not possible from these three lattices alone the authors estimate a continuum value of $m_\pi^c \approx 4$ GeV with an error of about 20%. In addition to the critical pion mass, also the critical hopping parameter κ_{Z_3} has been determined. It appears in fermion matrix for the Wilson quark action as

$$D(n_1|n_2) = \delta_{n_1, n_2} - \kappa \sum_{\mu=\pm 1}^{\pm 4} [(\not{K} - \gamma_\mu)U_\mu(n_1)\delta_{j+\hat{\mu}, n_2}] \quad (31)$$

and controls the bare quark mass m_b as

$$\kappa = \frac{1}{2(am_b + 4)}. \quad (32)$$

These results do not agree with those previously computed in Ref. [158]. Here reweighting from quenched QCD has been used to investigate the end-line in 2+1 flavor QCD. For the $N_f = 2$ and $N_t = 6$ case, the results differ by about 50%. Since the same lattice action has been used in both cases, the discrepancy is most likely related to the different methods and not to the cut off effects. Ref. [158] describes finite volume effects as well as effects related to the hopping parameter expansion which seems to shift the results in the direction of Ref. [157].

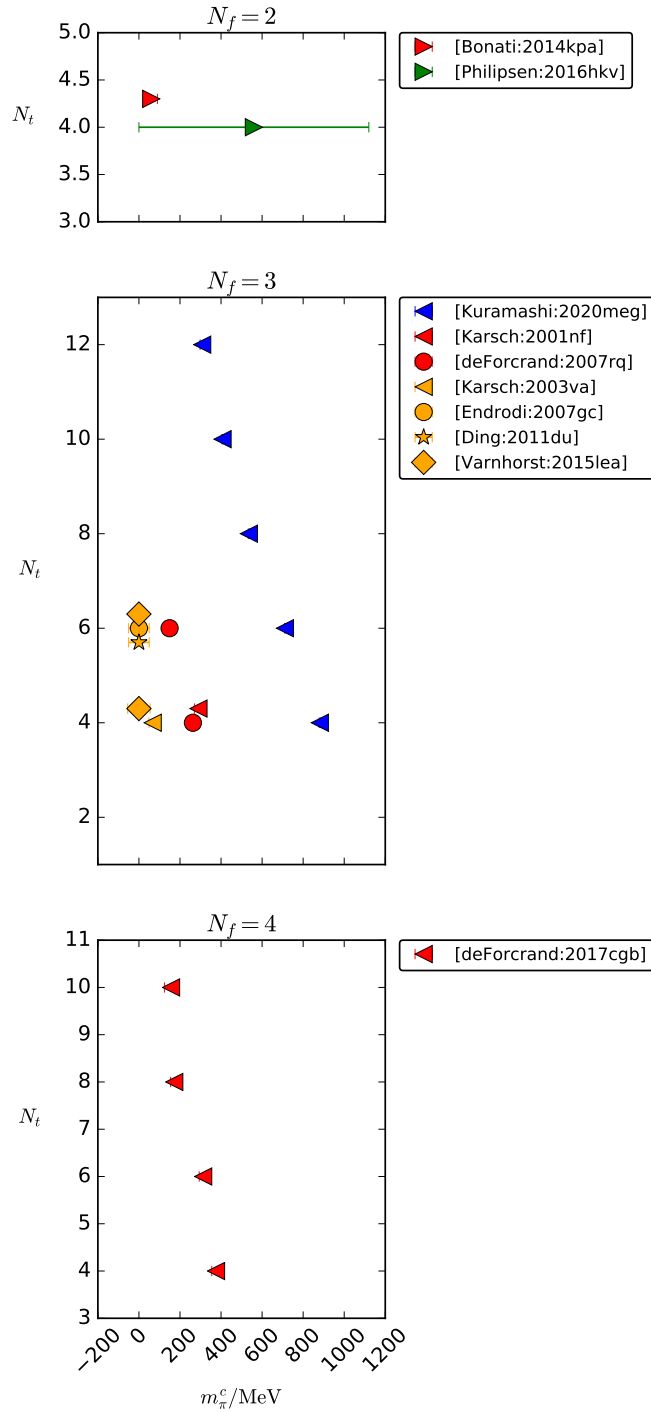


Figure 25: Overview over different available results for the critical pion mass in the Columbia plot for $N_f = 2, 3$ and 4 . Values are from Ref. [135–137, 145, 149, 150, 152–156]. The color of the points denotes the fermion type used in the simulations. Red stands for unimproved staggered, orange for improved staggered, green for unimproved Wilson and blue for improved Wilson quarks. Upper bounds are denoted by zero with the errorbar showing the bound. Values given without any errorbar are denoted with 50% relative error. Some values were converted to MeV using the value for the critical temperature from Ref. [150] $T_c = (156 \pm 8)$ MeV. Similar values for the same N_t have been shifted lightly for more clarity.

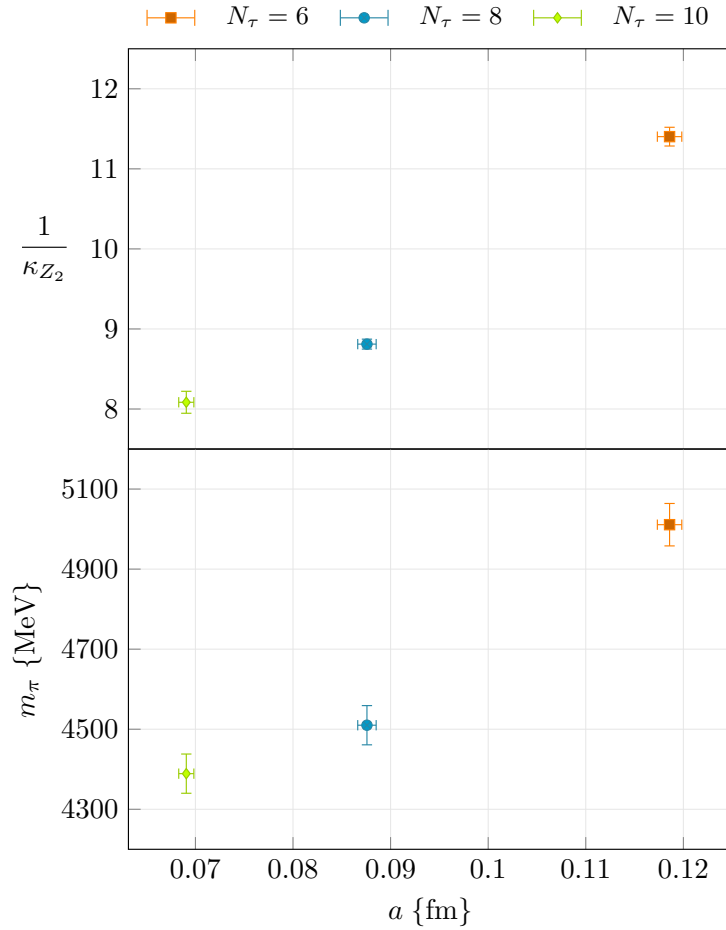


Figure 26: (Ref. [157]) Top: The critical value for the hopping parameter κ (see equations (32) and (31)) as a function of the lattice spacing. Bottom: Value of the critical pion mass as a function of the lattice spacing.

6 Magnetic fields

When dealing with heavy ion collision experiments, in addition to a finite chemical potential, also the effects of magnetic fields have to be considered (Ref. [159–161]). From zero temperature lattice QCD studies with staggered fermions (Ref. [162–164]) the so-called magnetic catalysis is found. It describes that the chiral condensate, which is an order parameter of the QCD chiral transition, increases with the strength of the magnetic field. From this it was derived that also the transition temperature increases with the magnetic field strength.

A recent study (Ref.[165]) investigated the chiral phase structure of three flavour QCD with a magnetic field on $N_t = 4$ lattices with four different volumes between $N_s = 8$ and $N_s = 24$. It uses a Wilson plaquette action with staggered fermions and pion masses of $m_\pi \approx 280$ MeV and two values of finite magnetic field strength. They find a strengthening in the transition, which turns to first order, when a magnetic field is added. The results for the chiral condensate for different magnetic field strengths and lattice volumes are shown in Fig. 27. The first order nature is derived both from the volume scaling as well as from meta stable states of the chiral condensate in the simulation stream. They also see an increase in the transition temperature with the magnetic field strength.

On the other hand, Ref. [166–171] find a decreasing transition temperature with growing magnetic fields. Here continuum extrapolations or improved actions were employed. It is assumed that the discrepancy is related to discretization artifacts (Ref. [165]). The decreasing of the transition temperature as well as the chiral condensate is called inverse magnetic catalysis. Most recently, Ref. [171] uses the HISQ quark action to study the effects of magnetic fields on a $16^3 \times 6$ lattice. They can observe the inverse magnetic catalysis even on a finite lattice.

To get a qualitative understanding of the processes leading to a magnetic catalysis or inverse magnetic catalysis, many model studies have been performed (Ref. [163, 172–183]). Lattice studies with heavy pion masses (Ref. [184, 185]) hint towards an explanation for the inverse magnetic catalysis unrelated to the decreasing of the chiral condensate, but related to the quark masses.

Ref. [184] uses 2+1 flavours of stout smeared staggered quarks on $N_t = 6$ lattices. They use pion masses up to $m_\pi \approx 600$ MeV and investigate the transition temperature as a function of the magnetic field strength. The transition temperature is determined both from the chiral condensate and the Polyakov loop leading to similar results. The chiral condensate for different strengths of the magnetic field and different pion masses is shown in figure 28 and figure 29. They find that, while the decrease of the transition temperature is present for all pion masses, the decrease of the chiral condensate, however, is not observable for the highest pion masses. This strengthens the idea that the inverse magnetic catalysis, the decrease of the chiral condensate, is not directly related to the transition temperature. The authors suggest that the decrease of the transition temperature might be a deconfinement catalysis (Ref. [186]).

Ref. [185] determines the transition point in the quark mass between magnetic catalysis and inverse catalysis further. They use the three stout smeared staggered fermions with

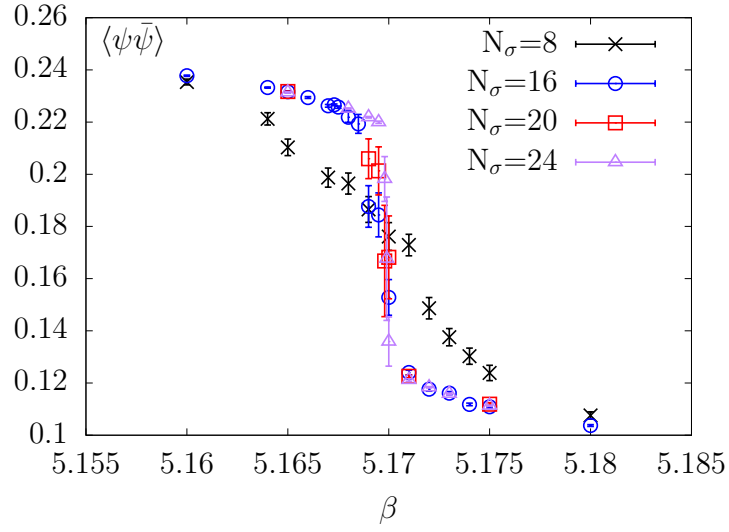
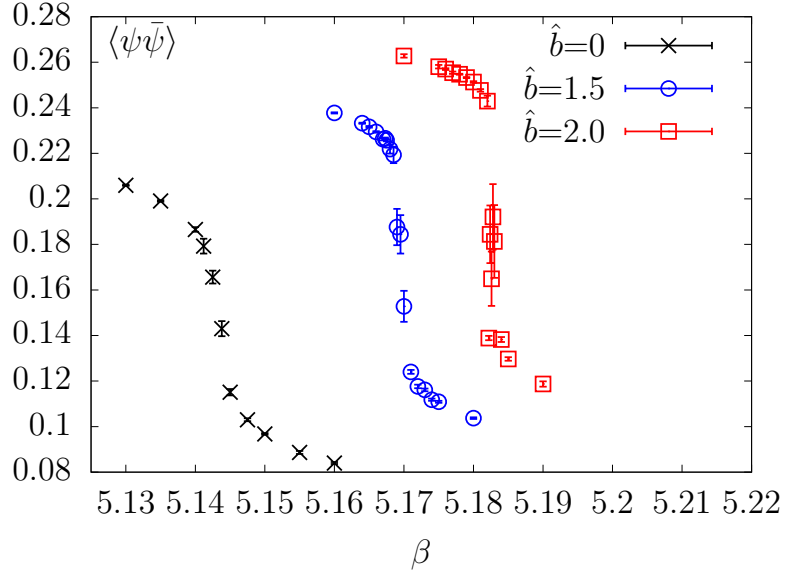


Figure 27: (Ref. [165]) Top: The chiral condensate on an $16^3 \times 4$ lattice for different magnetic field strengths $\hat{b} = a\sqrt{eB}$. Bottom: The chiral condensate for different volumes on lattices with temporal extent $N_t = 4$ at a magnetic field strength of $\hat{b} = a\sqrt{eB} = 1.5$.

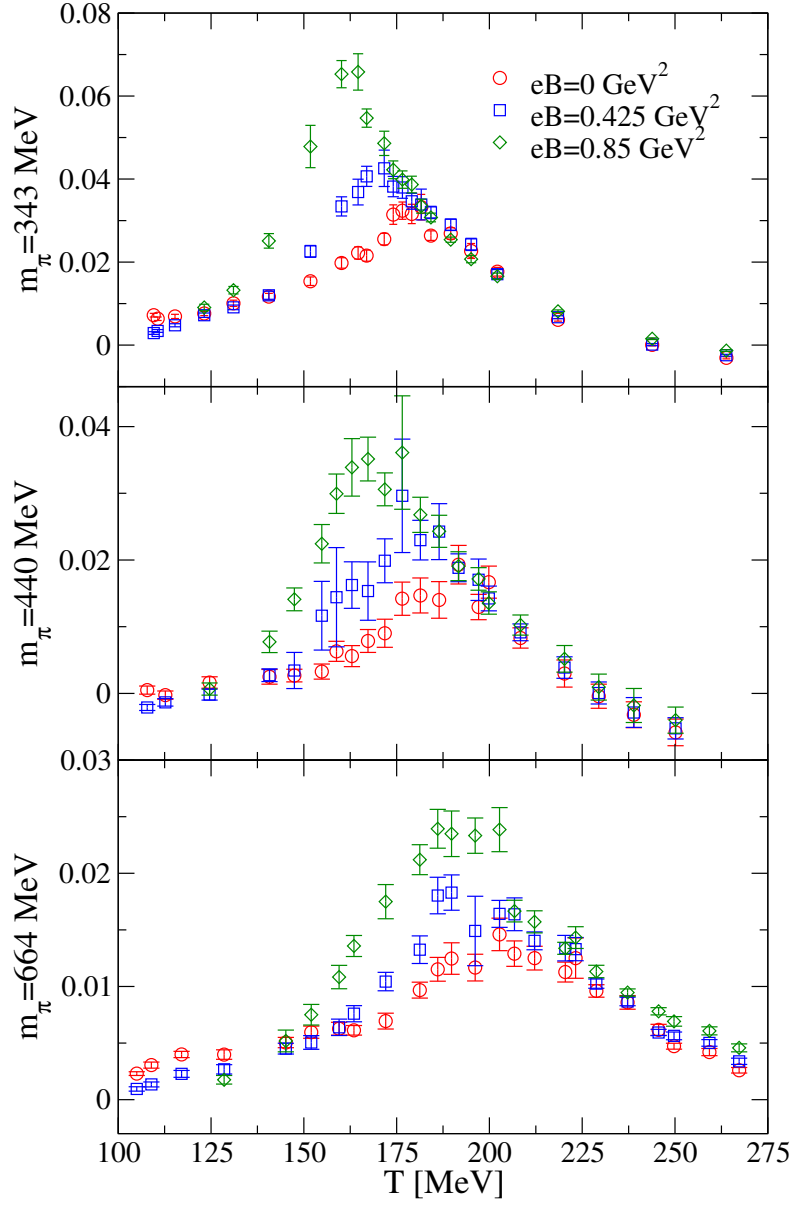


Figure 28: (Ref. [184]) The chiral susceptibility for different strengths of the magnetic field and different pion masses. Simulations were done with $N_f = 2 + 1$ stout smeared staggered fermions on $N_t = 6$ lattices. One can observe a decreasing peak position and therefore transition temperature for all pion masses.

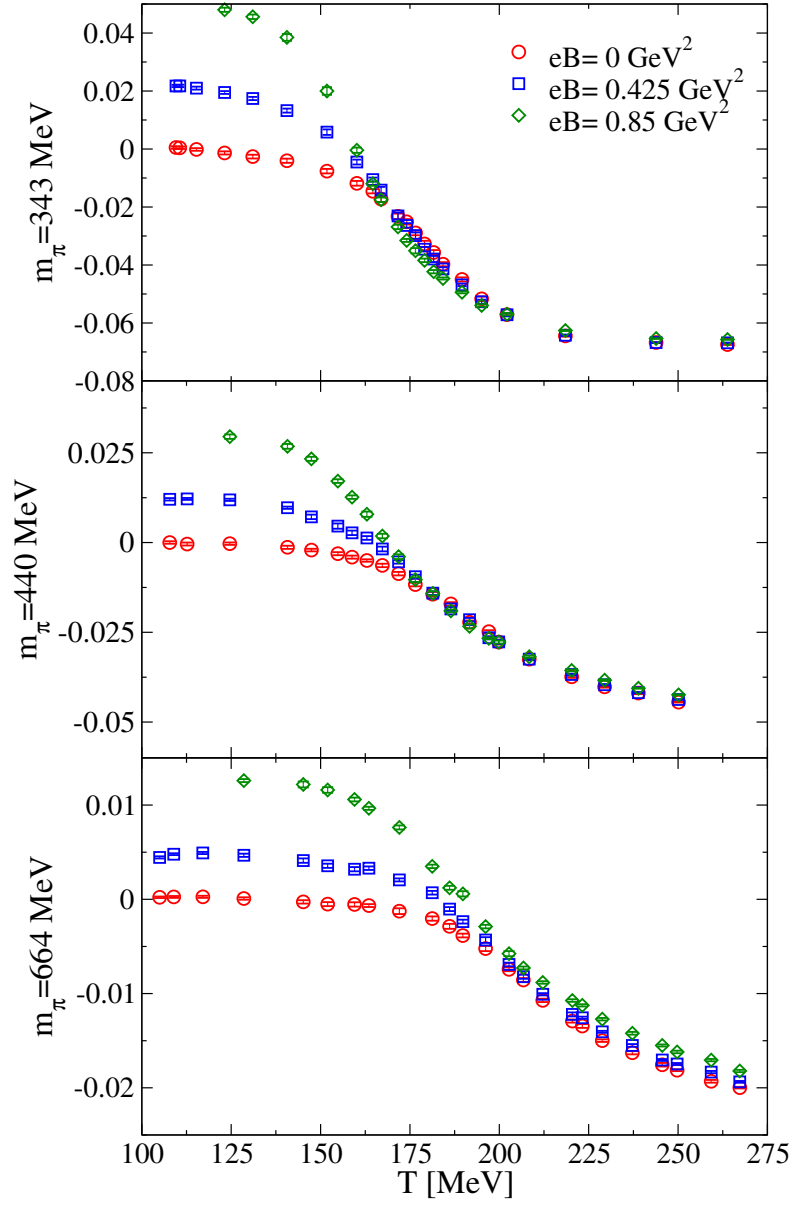


Figure 29: (Ref. [184]) The chiral condensate for different strengths of the magnetic field and different pion masses. Simulations were done with $N_f = 2 + 1$ stout smeared staggered fermions on $N_t = 6$ lattices. One can observe that while for the lightest pion mass the condensate decreases for a stronger magnetic field, it increases for the highest pion mass.

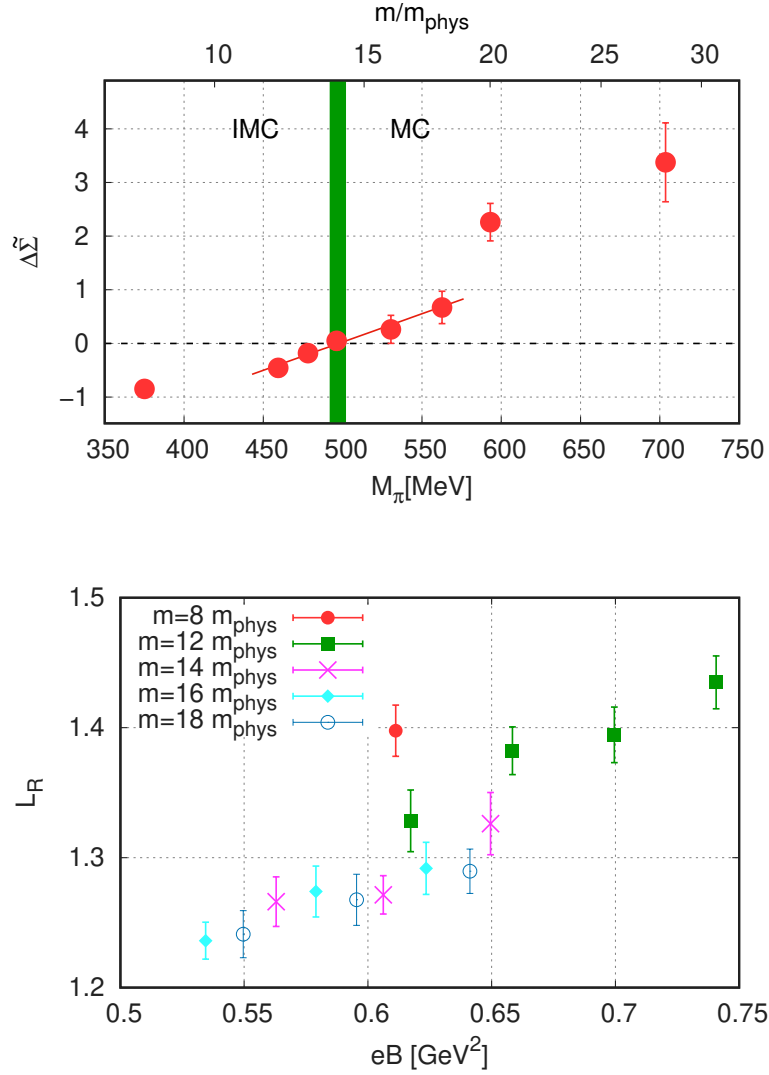


Figure 30: (Ref. [185]) Top: The dependence of the chiral condensate $\Delta\tilde{\Sigma}$ defined in equation (35) as a function of the pion mass in a magnetic field of $eB_0 = 0.6$ GeV. The green line separates the area of the inverse magnetic catalysis (IMC) from the area of the magnetic catalysis (MC) Bottom: The Polyakov loop ratio as defined in equation (37) as a function of the magnetic field close to the turning point between inverse magnetic catalysis and magnetic catalysis.

physical strange and variable light quark masses. The finite temperature and magnetic field simulations are performed on a $24^3 \times 6$ lattices. In addition four different zero temperature lattice simulations without a magnetic field were needed. To determine the mass \tilde{m} on the border between magnetic catalysis and inverse magnetic catalysis they look at the difference between the chiral condensate introduced by a magnetic field defined as

$$\Delta\Sigma(B, T, m) = \Sigma(B, T, m) - \Sigma(0, T, m) \quad (33)$$

$$= \frac{2m_{\text{phys}}}{M_\pi^2 F^2} [\langle \bar{\psi}\psi \rangle_{B, T, m} - \langle \bar{\psi}\psi \rangle_{0, T, m}], \quad (34)$$

for $eB_0 = 0.6 \text{ GeV}^2$ at the pseudo critical transition temperature T_c :

$$\Delta\tilde{\Sigma}(m) = \Delta\Sigma(B_0, T_c(m, B=0), m). \quad (35)$$

A sign change in $\Delta\tilde{\Sigma}$ than determines the value of \tilde{m} since for $\Delta\tilde{\Sigma} > 0$ the chiral condensate increases compared to the case without magnetic field while it decreases when $\Delta\tilde{\Sigma} < 0$. $\Delta\tilde{\Sigma}$ is shown in the top of Fig. 30, indicating $\frac{\tilde{m}}{m_{\text{phys}}} = 14.07 \pm 0.55$. This corresponds to a pion mass of $\tilde{m}_\pi = (497 \pm 4) \text{ MeV}$. In addition also the Polyakov loop

$$P = \frac{1}{V} \left\langle \sum_{\mathbf{x}} \Re \text{Tr} \prod_{t=0}^{N_t-1} U_4(\mathbf{x}, t) \right\rangle \quad (36)$$

from which the ratio

$$L_R = P(B, T, m) / P(0, T, m) \quad (37)$$

is defined, is investigated. Its behavior around \tilde{m} is shown in the top of Fig. 30.

The connections between the transition temperature, the quark masses and the chiral condensate in a magnetic field are further investigated in Ref. [164] for zero temperature. They connect the chiral condensate and the pion mass by the Gell-Mann-Oakes-Renner relation (Ref. [187]) for two flavours

$$(m_u + m_d) (\langle \bar{\psi}\psi \rangle_u + \langle \bar{\psi}\psi \rangle_d) = 2f_\pi^2 M_\pi^2 (1 - \delta_\pi), \quad (38)$$

and its extension to the 3-flavor case (Ref. [188]) with an additional strange quark

$$(m_s + m_d) (\langle \bar{\psi}\psi \rangle_s + \langle \bar{\psi}\psi \rangle_d) = 2f_K^2 M_K^2 (1 - \delta_K). \quad (39)$$

They use a 2 + 1-flavour HISQ quark action on a $32^3 \times 96$ lattice. The results for the light quark condensate defined as

$$\Sigma_l(B) = \frac{2m_l}{M_\pi^2 f_\pi^2} (\langle \bar{\psi}\psi \rangle_l(B \neq 0) - \langle \bar{\psi}\psi \rangle_l(B = 0)) + 1, \quad (40)$$

are shown in Fig. 31. They find that the Gell-Mann-Oakes-Renner relation for two flavours (equation (38)) has only corrections of about 6% when a magnetic field up to $eB = 3.35 \text{ GeV}^2$ is introduced. This illuminates the connection between the reduction of

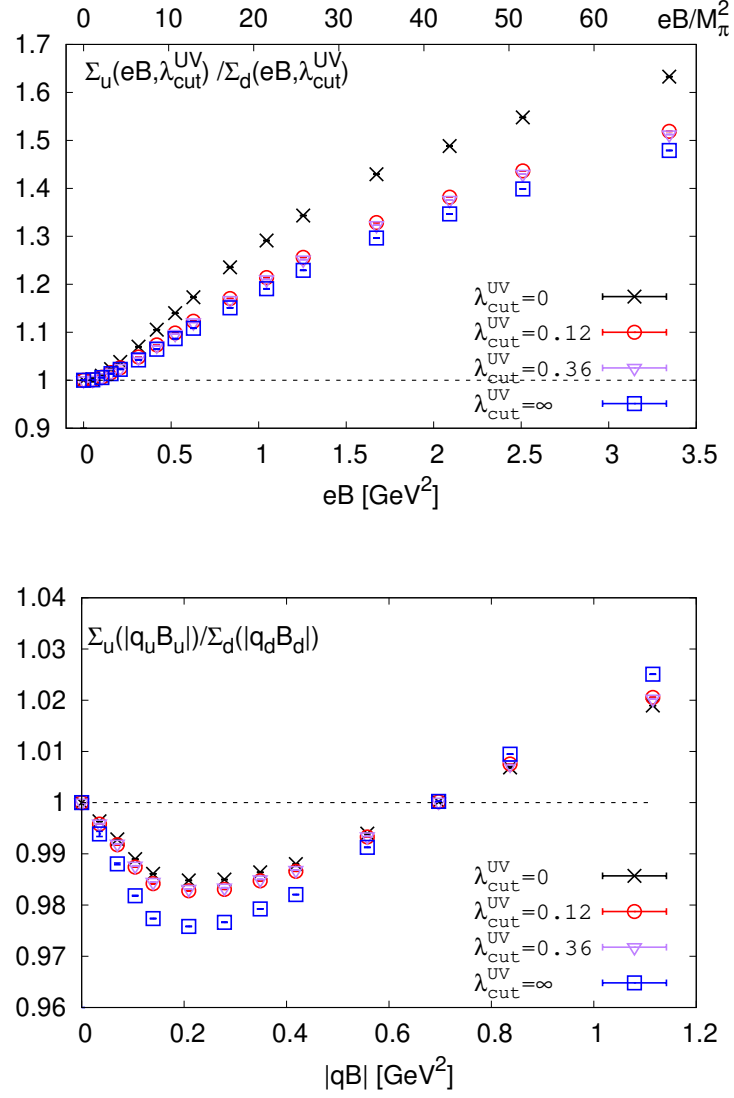


Figure 31: (Ref. [164]) Top: Ratio between the renormalized up quark and the down quark condensate $\Sigma_u(eB)/\Sigma_d(eB)$ as a function of eB . Bottom: Ratio between the renormalized up quark and the down quark condensate $\Sigma_u(eB)/\Sigma_d(eB)$ as a function of $|qB| = |q_u B_u| = |q_d B_d|$.

the transition temperature and the pion mass. For the three flavour case the corrections to the Gell-Mann-Oakes-Renner relation (equation (39)) are much larger namely up to 56%. Another recent investigation of the magnetic catalysis and the inverse magnetic catalysis can be found in Ref.[189], that study uses Dyson-Schwinger-equations instead of lattice QCD.

If one wants to match the conditions in heavy ion collisions in addition to the magnetic field a chemical potential should be considered. This causes the above discussed sign problem to reappear. Ref. [190] that studies the effect of a magnetic field and a finite baryon density with analytic continuation from imaginary μ_B finds that the inverse magnetic catalysis becomes slightly stronger with increased chemical potential.

7 Conclusion

The investigation of the QCD phase diagram, especially in relation to heavy ion collision experiments, remains a lively topic for lattice QCD calculations. With newly published results from LHC and RHIC as well as upcoming data from facilities like NICA, CBM and PARC-HI, a better understanding of the QCD phase diagram including various different influences that duplicate the situation in the colliders as well as possible, is needed.

After the introduction (section 1) and the brief description of the stages of a heavy ion collision experiment (section 2), this review started with the discussion of lattice QCD results at low, finite density (section 3). Accessing the phase diagram with a finite chemical potential is hindered by the infamous sign problem (section 3.1). It is the reason why, for now, continuum extrapolated, physical results, are only available as extrapolations (section 3.2). Because the QCD phase transition is an analytic crossover at $\mu = 0$, one can describe observables with an analytic function that is extrapolated to $\mu > 0$. There are two techniques for this kind of extrapolation which are commonly used. One can gain information on the μ dependence of the system either from calculating expansion coefficients from lattice simulations at zero chemical potential (Taylor method) or by describing simulation results at imaginary chemical potential with various functions. Both methods are by now agreeing well on various results. New publications include higher order coefficients on the Taylor expansion of the transition temperature, higher order cumulants of the baryon number distribution, which is used to compare to heavy ion collision experiments, as well as higher order cumulants of the baryon number distribution, which are used to compare to heavy ion collision experiments. In addition the possibility to find the QCD critical endpoint are under further investigation. There the development of new observables and techniques is necessary.

One method that is getting relatively close to direct lattice simulations at finite density are Complex Langevin simulations (section 3.3). These simulations are based on an evolution in a fictitious Langevin time to generate configurations with a complex measure. Here results are now available for different actions (both fermion and gauge). First comparisons to results from the Taylor expansion method are promising. However, for now results are only available with heavier than physical quark masses and on relatively

small lattices.

Another way to access finite density QCD are effective field theories (section 4), which also can be simulated on the lattice. This review focused on the results for heavy quarkonium (section 4.1). There the separation of scales in heavy quark bound states is used to integrate out various degrees of freedom. Lattice simulation can then employ NRQCD or pNRQCD to gain information of heavy quarkonium immersed in the quark gluon plasma.

Leaving the topic of finite density also zero density simulations show fascinating progress. By now there are a lot of results on the investigation of the Columbia plot (section 5). The Columbia plot summarizes the dependence of the type of the QCD transition (crossover, first or second order phase transition) on the lighter than physical quark masses. The lower left corner (section 5.1) poses a special computational challenge due to the light quark masses. Therefore, various techniques are employed to gain access to the first order region located there and its critical boundary (section 5.2 and section 5.3). For the case of three degenerate light quarks results are now available on up to $N_t = 12$ lattices with improved Wilson quarks. However, the continuum extrapolation cannot be carried out yet. This review is therefore restricted to an overview (section 5.4) of the available results for different discretizations. Also the upper right corner of the Columbia plot has been investigated recently (section 5.5). Here the current estimate for the critical pion mass in the continuum is $m_\pi^c \approx 4$ GeV with an error of about 20%.

Finally this review discusses recent results on the influence of a magnetic field (section 6). Like the inclusion of a chemical potential, these effects are relevant for heavy ion collision experiments. An important topic is the distinction between the magnetic catalysis and inverse catalysis which has been related to the light quark masses. Here the lattice results are not in agreement with the common expectation from perturbation theory.

Investigating the QCD phase diagram is a fascinating topic from a purely theoretical point of view. However, many recent results in finite temperature lattice QCD are linked to heavy ion collision experiments. The experimental progress on the quark gluon plasma allows on the one hand to confirm the theoretical predictions made by QCD. On the other hand, the computation from lattice QCD are needed by experiments to understand the observations made by the detectors and link them to different stages of collision. This can be done either directly by lattice QCD or through different models or effective theories. In any case the continuation of the experimental heavy ion collision programs will provide interesting checks and challenges for finite temperature lattice QCD calculations.

Acknowledgments

The author thanks Lukas Varnhorst for proofreading and discussion. The project leading to this publication has received funding from Excellence Initiative of Aix-Marseille University - A*MIDEX, a French “Investissements d’Avenir” programme, AMX-18-ACE-005.

References

- [1] Y. Aoki, G. Endrodi, Z. Fodor, S. D. Katz, and K. K. Szabo. The Order of the quantum chromodynamics transition predicted by the standard model of particle physics. *Nature*, 443:675–678, 2006.
- [2] Y. Aoki, Z. Fodor, S.D. Katz, and K.K. Szabo. The QCD transition temperature: Results with physical masses in the continuum limit. *Phys. Lett. B*, 643:46–54, 2006.
- [3] Y. Aoki, Szabolcs Borsanyi, Stephan Durr, Zoltan Fodor, Sandor D. Katz, Stefan Krieg, and Kalman K. Szabo. The QCD transition temperature: results with physical masses in the continuum limit II. *JHEP*, 06:088, 2009.
- [4] Szabolcs Borsanyi, Zoltan Fodor, Christian Hoelbling, Sandor D Katz, Stefan Krieg, Claudia Ratti, and Kalman K. Szabo. Is there still any T_c mystery in lattice QCD? Results with physical masses in the continuum limit III. *JHEP*, 09:073, 2010.
- [5] Tanmoy Bhattacharya et al. QCD Phase Transition with Chiral Quarks and Physical Quark Masses. *Phys. Rev. Lett.*, 113(8):082001, 2014.
- [6] A. Bazavov et al. The chiral and deconfinement aspects of the QCD transition. *Phys. Rev.*, D85:054503, 2012.
- [7] Ian M. Barbour, Susan E. Morrison, Elyakum G. Klepfish, John B. Kogut, and Maria-Paola Lombardo. Results on finite density QCD. *Nucl. Phys. B Proc. Suppl.*, 60:220–234, 1998.
- [8] Z. Fodor and S. D. Katz. A New method to study lattice QCD at finite temperature and chemical potential. *Phys. Lett.*, B534:87–92, 2002.
- [9] Z. Fodor and S. D. Katz. Lattice determination of the critical point of QCD at finite T and mu. *JHEP*, 03:014, 2002.
- [10] F. Csikor, G.I. Egri, Z. Fodor, S.D. Katz, K.K. Szabo, and A.I. Toth. The QCD equation of state at finite T and mu. *Nucl. Phys. B Proc. Suppl.*, 119:547–549, 2003.
- [11] Zoltan Fodor, Sandor D. Katz, and Christian Schmidt. The Density of states method at non-zero chemical potential. *JHEP*, 03:121, 2007.
- [12] Andrei Alexandru, C. Gatttringer, H. P. Schadler, K. Splittorff, and J.J.M. Verbaarschot. Distribution of Canonical Determinants in QCD. *Phys. Rev. D*, 91(7):074501, 2015.
- [13] Andrei Alexandru, Manfred Faber, Ivan Horvath, and Keh-Fei Liu. Lattice QCD at finite density via a new canonical approach. *Phys. Rev. D*, 72:114513, 2005.

- [14] Slavo Kratochvila and Philippe de Forcrand. The Canonical approach to finite density QCD. *PoS*, LAT2005:167, 2006.
- [15] Shinji Ejiri. Canonical partition function and finite density phase transition in lattice QCD. *Phys. Rev. D*, 78:074507, 2008.
- [16] Christof Gattringer. New developments for dual methods in lattice field theory at non-zero density. *PoS*, LATTICE2013:002, 2014.
- [17] Luigi Scorzato. The Lefschetz thimble and the sign problem. *PoS*, LATTICE2015:016, 2016.
- [18] Andrei Alexandru, Gökçe Basar, and Paulo Bedaque. Monte Carlo algorithm for simulating fermions on Lefschetz thimbles. *Phys. Rev. D*, 93(1):014504, 2016.
- [19] Alexander Rothkopf. Heavy Quarkonium in Extreme Conditions. *Phys. Rept.*, 858:1–117, 2020.
- [20] Francois Gelis, Edmond Iancu, Jamal Jalilian-Marian, and Raju Venugopalan. The Color Glass Condensate. *Ann. Rev. Nucl. Part. Sci.*, 60:463–489, 2010.
- [21] F. Gelis. Color Glass Condensate and Glasma. *Int. J. Mod. Phys. A*, 28:1330001, 2013.
- [22] Dirk H. Rischke. The Quark gluon plasma in equilibrium. *Prog. Part. Nucl. Phys.*, 52:197–296, 2004.
- [23] P. Hasenfratz and F. Karsch. Chemical Potential on the Lattice. *Phys. Lett. B*, 125:308–310, 1983.
- [24] C. R. Allton, S. Ejiri, S. J. Hands, O. Kaczmarek, F. Karsch, E. Laermann, C. Schmidt, and L. Scorzato. The QCD thermal phase transition in the presence of a small chemical potential. *Phys. Rev.*, D66:074507, 2002.
- [25] C. R. Allton, M. Doring, S. Ejiri, S. J. Hands, O. Kaczmarek, F. Karsch, E. Laermann, and K. Redlich. Thermodynamics of two flavor QCD to sixth order in quark chemical potential. *Phys. Rev.*, D71:054508, 2005.
- [26] R. V. Gavai and Sourendu Gupta. QCD at finite chemical potential with six time slices. *Phys. Rev.*, D78:114503, 2008.
- [27] S. Basak et al. QCD equation of state at non-zero chemical potential. *PoS*, LATTICE2008:171, 2008.
- [28] O. Kaczmarek, F. Karsch, E. Laermann, C. Miao, S. Mukherjee, P. Petreczky, C. Schmidt, W. Soeldner, and W. Unger. Phase boundary for the chiral transition in (2+1) -flavor QCD at small values of the chemical potential. *Phys. Rev.*, D83:014504, 2011.

- [29] Erhard Seiler, Denes Sexty, and Ion-Olimpiu Stamatescu. Gauge cooling in complex Langevin for QCD with heavy quarks. *Phys. Lett. B*, 723:213–216, 2013.
- [30] Dénes Sexty. Simulating full QCD at nonzero density using the complex Langevin equation. *Phys. Lett. B*, 729:108–111, 2014.
- [31] Szabolcs Borsanyi, Zoltan Fodor, Sandor D. Katz, Stefan Krieg, Claudia Ratti, and Kalman Szabo. Fluctuations of conserved charges at finite temperature from lattice QCD. *JHEP*, 01:138, 2012.
- [32] Sz. Borsanyi, G. Endrodi, Z. Fodor, S.D. Katz, S. Krieg, C. Ratti, and K.K. Szabo. QCD equation of state at nonzero chemical potential: continuum results with physical quark masses at order mu^2 . *JHEP*, 08:053, 2012.
- [33] R. Bellwied, S. Borsanyi, Z. Fodor, S. D. Katz, A. Pasztor, C. Ratti, and K. K. Szabo. Fluctuations and correlations in high temperature QCD. *Phys. Rev.*, D92(11):114505, 2015.
- [34] H. T. Ding, Swagato Mukherjee, H. Ohno, P. Petreczky, and H. P. Schadler. Diagonal and off-diagonal quark number susceptibilities at high temperatures. *Phys. Rev. D*, 92(7):074043, 2015.
- [35] A. Bazavov et al. The QCD Equation of State to $\mathcal{O}(\mu_B^6)$ from Lattice QCD. *Phys. Rev.*, D95(5):054504, 2017.
- [36] A. Bazavov et al. Chiral crossover in QCD at zero and non-zero chemical potentials. *Phys. Lett.*, B795:15–21, 2019.
- [37] A. Bazavov et al. Skewness, kurtosis, and the fifth and sixth order cumulants of net baryon-number distributions from lattice QCD confront high-statistics STAR data. *Phys. Rev. D*, 101(7):074502, 2020.
- [38] Claudio Bonati, Massimo D’Elia, Francesco Negro, Francesco Sanfilippo, and Kevin Zambello. Curvature of the pseudocritical line in QCD: Taylor expansion matches analytic continuation. *Phys. Rev. D*, 98(5):054510, 2018.
- [39] G. Endrodi, Z. Fodor, S. D. Katz, and K. K. Szabo. The QCD phase diagram at nonzero quark density. *JHEP*, 04:001, 2011.
- [40] Philippe de Forcrand and Owe Philipsen. The QCD phase diagram for small densities from imaginary chemical potential. *Nucl. Phys.*, B642:290–306, 2002.
- [41] Massimo D’Elia and Maria-Paola Lombardo. Finite density QCD via imaginary chemical potential. *Phys. Rev.*, D67:014505, 2003.
- [42] Massimo D’Elia and Francesco Sanfilippo. Thermodynamics of two flavor QCD from imaginary chemical potentials. *Phys. Rev. D*, 80:014502, 2009.

- [43] Paolo Cea, Leonardo Cosmai, and Alessandro Papa. Critical line of 2+1 flavor QCD. *Phys. Rev. D*, 89(7):074512, 2014.
- [44] Claudio Bonati, Philippe de Forcrand, Massimo D’Elia, Owe Philipsen, and Francesco Sanfilippo. Chiral phase transition in two-flavor QCD from an imaginary chemical potential. *Phys. Rev. D*, 90(7):074030, 2014.
- [45] Paolo Cea, Leonardo Cosmai, and Alessandro Papa. Critical line of 2+1 flavor QCD: Toward the continuum limit. *Phys. Rev.*, D93(1):014507, 2016.
- [46] Claudio Bonati, Massimo D’Elia, Marco Mariti, Michele Mesiti, Francesco Negro, and Francesco Sanfilippo. Curvature of the chiral pseudocritical line in QCD: Continuum extrapolated results. *Phys. Rev.*, D92(5):054503, 2015.
- [47] R. Bellwied, S. Borsanyi, Z. Fodor, J. Guenther, S. D. Katz, C. Ratti, and K. K. Szabo. The QCD phase diagram from analytic continuation. *Phys. Lett.*, B751:559–564, 2015.
- [48] Massimo D’Elia, Giuseppe Gagliardi, and Francesco Sanfilippo. Higher order quark number fluctuations via imaginary chemical potentials in $N_f = 2 + 1$ QCD. *Phys. Rev.*, D95(9):094503, 2017.
- [49] J. N. Guenther, R. Bellwied, S. Borsanyi, Z. Fodor, S. D. Katz, A. Pasztor, C. Ratti, and K. K. Szabó. The QCD equation of state at finite density from analytical continuation. *Nucl. Phys.*, A967:720–723, 2017.
- [50] Paolo Alba et al. Constraining the hadronic spectrum through QCD thermodynamics on the lattice. *Phys. Rev. D*, 96(3):034517, 2017.
- [51] Volodymyr Vovchenko, Attila Pasztor, Zoltan Fodor, Sandor D. Katz, and Horst Stoecker. Repulsive baryonic interactions and lattice QCD observables at imaginary chemical potential. *Phys. Lett. B*, 775:71–78, 2017.
- [52] Szabolcs Borsanyi, Zoltan Fodor, Jana N. Guenther, Sandor K. Katz, Kalman K. Szabo, Attila Pasztor, Israel Portillo, and Claudia Ratti. Higher order fluctuations and correlations of conserved charges from lattice QCD. 2018.
- [53] Szabolcs Borsanyi, Zoltan Fodor, Jana N. Guenther, Ruben Kara, Sandor D. Katz, Paolo Parotto, Attila Pasztor, Claudia Ratti, and Kalman K. Szabo. The QCD crossover at finite chemical potential from lattice simulations. 2020.
- [54] René Bellwied, Szabolcs Borsányi, Zoltán Fodor, Jana Günther, Sándor D. Katz, Kálmán K. Szabó, Claudia Ratti, and Attila Pasztor. Fluctuations and correlations in finite temperature QCD. *PoS*, ICHEP2016:369, 2016.
- [55] Attila Pásztor, Zsolt Szép, and Gergely Markó. Apparent convergence of Padé approximants for the crossover line in finite density QCD. 10 2020.

- [56] Patrick Steinbrecher. The QCD crossover at zero and non-zero baryon densities from Lattice QCD. *Nucl. Phys. A*, 982:847–850, 2019.
- [57] Philipp Isserstedt, Michael Buballa, Christian S. Fischer, and Pascal J. Gunkel. Baryon number fluctuations in the QCD phase diagram from Dyson-Schwinger equations. *Phys. Rev.*, D100(7):074011, 2019.
- [58] A. Andronic, P. Braun-Munzinger, and J. Stachel. Hadron production in central nucleus-nucleus collisions at chemical freeze-out. *Nucl. Phys.*, A772:167–199, 2006.
- [59] Francesco Becattini, Marcus Bleicher, Thorsten Kollegger, Tim Schuster, Jan Steinheimer, and Reinhard Stock. Hadron Formation in Relativistic Nuclear Collisions and the QCD Phase Diagram. *Phys. Rev. Lett.*, 111:082302, 2013.
- [60] Paolo Alba, Wanda Alberico, Rene Bellwied, Marcus Bluhm, Valentina Mantonani Sarti, Marlene Nahrgang, and Claudia Ratti. Freeze-out conditions from net-proton and net-charge fluctuations at RHIC. *Phys. Lett.*, B738:305–310, 2014.
- [61] V. Vovchenko, V. V. Begun, and M. I. Gorenstein. Hadron multiplicities and chemical freeze-out conditions in proton-proton and nucleus-nucleus collisions. *Phys. Rev.*, C93(6):064906, 2016.
- [62] L. Adamczyk et al. Bulk Properties of the Medium Produced in Relativistic Heavy-Ion Collisions from the Beam Energy Scan Program. *Phys. Rev.*, C96(4):044904, 2017.
- [63] Y. Hatta and M.A. Stephanov. Proton number fluctuation as a signal of the QCD critical endpoint. *Phys. Rev. Lett.*, 91:102003, 2003. [Erratum: *Phys.Rev.Lett.* 91, 129901 (2003)].
- [64] M.A. Stephanov. Non-Gaussian fluctuations near the QCD critical point. *Phys. Rev. Lett.*, 102:032301, 2009.
- [65] B. Friman, F. Karsch, K. Redlich, and V. Skokov. Fluctuations as probe of the QCD phase transition and freeze-out in heavy ion collisions at LHC and RHIC. *Eur. Phys. J. C*, 71:1694, 2011.
- [66] Adam Miklos Halasz, A.D. Jackson, R.E. Shrock, Misha A. Stephanov, and J.J.M. Verbaarschot. On the phase diagram of QCD. *Phys. Rev. D*, 58:096007, 1998.
- [67] Misha A. Stephanov, K. Rajagopal, and Edward V. Shuryak. Event-by-event fluctuations in heavy ion collisions and the QCD critical point. *Phys. Rev.*, D60:114028, 1999.
- [68] M. Cheng et al. The QCD equation of state with almost physical quark masses. *Phys. Rev.*, D77:014511, 2008.
- [69] A. Bazavov et al. Skewness and kurtosis of net baryon-number distributions at small values of the baryon chemical potential. 2017.

- [70] Frithjof Karsch. Determination of Freeze-out Conditions from Lattice QCD Calculations. *Central Eur. J. Phys.*, 10:1234–1237, 2012.
- [71] A. Bazavov et al. Freeze-out Conditions in Heavy Ion Collisions from QCD Thermodynamics. *Phys. Rev. Lett.*, 109:192302, 2012.
- [72] S. Borsanyi, Z. Fodor, S. D. Katz, S. Krieg, C. Ratti, and K. K. Szabo. Freeze-out parameters: lattice meets experiment. *Phys. Rev. Lett.*, 111:062005, 2013.
- [73] S. Borsanyi, Z. Fodor, S. D. Katz, S. Krieg, C. Ratti, and K. K. Szabo. Freeze-out parameters from electric charge and baryon number fluctuations: is there consistency? *Phys. Rev. Lett.*, 113:052301, 2014.
- [74] Claudia Ratti. Lattice QCD and heavy ion collisions: a review of recent progress. *Rept. Prog. Phys.*, 81(8):084301, 2018.
- [75] J. Adam et al. Net-proton number fluctuations and the Quantum Chromodynamics critical point. 1 2020.
- [76] Toshihiro Nonaka. Measurement of the Sixth-Order Cumulant of Net-Proton Distributions in Au+Au Collisions from the STAR Experiment. In *28th International Conference on Ultrarelativistic Nucleus-Nucleus Collisions*, 2 2020.
- [77] Rene Bellwied, Szabolcs Borsanyi, Zoltan Fodor, Jana N. Guenther, Jacquelyn Noronha-Hostler, Paolo Parotto, Attila Pasztor, Claudia Ratti, and Jamie M. Stafford. Off-diagonal correlators of conserved charges from lattice QCD and how to relate them to experiment. *Phys. Rev. D*, 101(3):034506, 2020.
- [78] V.V. Begun, Mark I. Gorenstein, M. Hauer, V.P. Konchakovski, and O.S. Zozulya. Multiplicity Fluctuations in Hadron-Resonance Gas. *Phys. Rev. C*, 74:044903, 2006.
- [79] Masakiyo Kitazawa and Masayuki Asakawa. Revealing baryon number fluctuations from proton number fluctuations in relativistic heavy ion collisions. *Phys. Rev. C*, 85:021901, 2012.
- [80] Masakiyo Kitazawa and Masayuki Asakawa. Relation between baryon number fluctuations and experimentally observed proton number fluctuations in relativistic heavy ion collisions. *Phys. Rev. C*, 86:024904, 2012. [Erratum: *Phys.Rev.C* 86, 069902 (2012)].
- [81] Matteo Giordano and Attila Pásztor. Reliable estimation of the radius of convergence in finite density QCD. *Phys. Rev. D*, 99(11):114510, 2019.
- [82] T.D. Lee and Chen-Ning Yang. Statistical theory of equations of state and phase transitions. 2. Lattice gas and Ising model. *Phys. Rev.*, 87:410–419, 1952.
- [83] A. Hasenfratz and D. Toussaint. Canonical ensembles and nonzero density quantum chromodynamics. *Nucl. Phys. B*, 371:539–549, 1992.

- [84] Z. Fodor and S. D. Katz. Critical point of QCD at finite T and mu, lattice results for physical quark masses. *JHEP*, 04:050, 2004.
- [85] Julia Danzer and Christof Gattringer. Winding expansion techniques for lattice QCD with chemical potential. *Phys. Rev. D*, 78:114506, 2008.
- [86] Andrei Alexandru and Urs Wenger. QCD at non-zero density and canonical partition functions with Wilson fermions. *Phys. Rev. D*, 83:034502, 2011.
- [87] Matteo Giordano, Kornel Kapas, Sandor D. Katz, Daniel Nogradi, and Attila Pasztor. Radius of convergence in lattice QCD at finite μ_B with rooted staggered fermions. *Phys. Rev. D*, 101(7):074511, 2020.
- [88] Matteo Giordano, Kornel Kapas, Sandor D. Katz, Daniel Nogradi, and Attila Pasztor. New approach to lattice QCD at finite density; results for the critical end point on coarse lattices. *JHEP*, 05:088, 2020.
- [89] Felipe Attanasio, Benjamin Jäger, and Felix P.G. Ziegler. Complex Langevin and the QCD phase diagram: Recent developments. 5 2020.
- [90] Jan Ambjorn and S.K. Yang. Numerical Problems in Applying the Langevin Equation to Complex Effective Actions. *Phys. Lett. B*, 165:140, 1985.
- [91] John R. Klauder and Wesley P. Petersen. SPECTRUM OF CERTAIN NON-SELFADJOINT OPERATORS AND SOLUTIONS OF LANGEVIN EQUATIONS WITH COMPLEX DRIFT. *J. Stat. Phys.*, 39:53–72, 1985.
- [92] H. Q. Lin and J. E. Hirsch. Monte carlo versus langevin methods for nonpositive definite weights. *Phys. Rev. B*, 34:1964–1967, Aug 1986.
- [93] Jan Ambjorn, M. Flensburg, and C. Peterson. The Complex Langevin Equation and Monte Carlo Simulations of Actions With Static Charges. *Nucl. Phys. B*, 275:375–397, 1986.
- [94] Gert Aarts, Lorenzo Bongiovanni, Erhard Seiler, Denes Sexty, and Ion-Olimpiu Stamatescu. Controlling complex Langevin dynamics at finite density. *Eur. Phys. J. A*, 49:89, 2013.
- [95] Juergen Berges and Denes Sexty. Real-time gauge theory simulations from stochastic quantization with optimized updating. *Nucl. Phys. B*, 799:306–329, 2008.
- [96] Gert Aarts, Frank A. James, Erhard Seiler, and Ion-Olimpiu Stamatescu. Adaptive stepsize and instabilities in complex Langevin dynamics. *Phys. Lett. B*, 687:154–159, 2010.
- [97] Felipe Attanasio and Benjamin Jäger. Dynamical stabilisation of complex Langevin simulations of QCD. *Eur. Phys. J. C*, 79(1):16, 2019.

- [98] Jun Nishimura and Shinji Shimasaki. New Insights into the Problem with a Singular Drift Term in the Complex Langevin Method. *Phys. Rev. D*, 92(1):011501, 2015.
- [99] Gert Aarts, Erhard Seiler, Denes Sexty, and Ion-Olimpiu Stamatescu. Complex Langevin dynamics and zeroes of the fermion determinant. *JHEP*, 05:044, 2017. [Erratum: *JHEP* 01, 128 (2018)].
- [100] Keitaro Nagata, Jun Nishimura, and Shinji Shimasaki. Argument for justification of the complex Langevin method and the condition for correct convergence. *Phys. Rev. D*, 94(11):114515, 2016.
- [101] Keitaro Nagata, Jun Nishimura, and Shinji Shimasaki. Testing the criterion for correct convergence in the complex Langevin method. *JHEP*, 05:004, 2018.
- [102] Manuel Scherzer, Erhard Seiler, Dénes Sexty, and Ion-Olimpiu Stamatescu. Complex Langevin and boundary terms. *Phys. Rev. D*, 99(1):014512, 2019.
- [103] Shoichiro Tsutsui, Yuta Ito, Hideo Matsufuru, Jun Nishimura, Shinji Shimasaki, and Asato Tsuchiya. Exploring the QCD phase diagram at finite density by the complex Langevin method on a $16^3 \times 32$ lattice. *PoS, LATTICE2019*:151, 2019.
- [104] Dénes Sexty. Calculating the equation of state of dense quark-gluon plasma using the complex Langevin equation. *Phys. Rev. D*, 100(7):074503, 2019.
- [105] M. Scherzer, D. Sexty, and I.-O. Stamatescu. Deconfinement transition line with the complex Langevin equation up to $\mu/T \sim 5$. *Phys. Rev. D*, 102(1):014515, 2020.
- [106] Yuta Ito, Hideo Matsufuru, Jun Nishimura, Shinji Shimasaki, Asato Tsuchiya, and Shoichiro Tsutsui. Exploring the phase diagram of finite density QCD at low temperature by the complex Langevin method. *PoS, LATTICE2018*:146, 2018.
- [107] Yuta Ito, Hideo Matsufuru, Yusuke Namekawa, Jun Nishimura, Shinji Shimasaki, Asato Tsuchiya, and Shoichiro Tsutsui. Complex Langevin calculations in QCD at finite density. *JHEP*, 10:144, 2020.
- [108] J.B. Kogut and D.K. Sinclair. Applying Complex Langevin Simulations to Lattice QCD at Finite Density. *Phys. Rev. D*, 100(5):054512, 2019.
- [109] F. Karsch, E. Laermann, P. Petreczky, and S. Stickan. Infinite temperature limit of meson spectral functions calculated on the lattice. *Phys. Rev. D*, 68:014504, 2003.
- [110] Gert Aarts and Jose M. Martinez Resco. Continuum and lattice meson spectral functions at nonzero momentum and high temperature. *Nucl. Phys. B*, 726:93–108, 2005.
- [111] W.E. Caswell and G.P. Lepage. Effective Lagrangians for Bound State Problems in QED, QCD, and Other Field Theories. *Phys. Lett. B*, 167:437–442, 1986.

- [112] Nora Brambilla, Antonio Pineda, Joan Soto, and Antonio Vairo. Potential NRQCD: An Effective theory for heavy quarkonium. *Nucl. Phys. B*, 566:275, 2000.
- [113] Alexei Bazavov, Nora Brambilla, Peter Petreczky, Antonio Vairo, and Johannes Heinrich Weber. Color screening in (2+1)-flavor QCD. *Phys. Rev. D*, 98(5):054511, 2018.
- [114] Gert Aarts, Chris Allton, Tim Harris, Seyong Kim, Maria Paola Lombardo, Sinéad M. Ryan, and Jon-Ivar Skullerud. The bottomonium spectrum at finite temperature from $N_f = 2 + 1$ lattice QCD. *JHEP*, 07:097, 2014.
- [115] G. Aarts, C. Allton, S. Kim, M.P. Lombardo, S.M. Ryan, and J.-I. Skullerud. Melting of P wave bottomonium states in the quark-gluon plasma from lattice NRQCD. *JHEP*, 12:064, 2013.
- [116] Gert Aarts, Chris Allton, Seyong Kim, Maria Paola Lombardo, Mehmet B. Oktay, Sinead M. Ryan, D.K. Sinclair, and Jon-Ivar Skullerud. S wave bottomonium states moving in a quark-gluon plasma from lattice NRQCD. *JHEP*, 03:084, 2013.
- [117] G. Aarts, C. Allton, S. Kim, M.P. Lombardo, M.B. Oktay, S.M. Ryan, D.K. Sinclair, and J.I. Skullerud. What happens to the Upsilon and η_c in the quark-gluon plasma? Bottomonium spectral functions from lattice QCD. *JHEP*, 11:103, 2011.
- [118] G. Aarts, S. Kim, M.P. Lombardo, M.B. Oktay, S.M. Ryan, D.K. Sinclair, and J.-I. Skullerud. Bottomonium above deconfinement in lattice nonrelativistic QCD. *Phys. Rev. Lett.*, 106:061602, 2011.
- [119] Seyong Kim, Peter Petreczky, and Alexander Rothkopf. Lattice NRQCD study of S- and P-wave bottomonium states in a thermal medium with $N_f = 2 + 1$ light flavors. *Phys. Rev. D*, 91:054511, 2015.
- [120] Seyong Kim, Peter Petreczky, and Alexander Rothkopf. Quarkonium in-medium properties from realistic lattice NRQCD. *JHEP*, 11:088, 2018.
- [121] Rasmus Larsen, Stefan Meinel, Swagato Mukherjee, and Peter Petreczky. Excited bottomonia in quark-gluon plasma from lattice QCD. *Phys. Lett. B*, 800:135119, 2020.
- [122] Rasmus Larsen, Stefan Meinel, Swagato Mukherjee, and Peter Petreczky. Thermal broadening of bottomonia: Lattice nonrelativistic QCD with extended operators. *Phys. Rev. D*, 100(7):074506, 2019.
- [123] David Lafferty and Alexander Rothkopf. Improved Gauss law model and in-medium heavy quarkonium at finite density and velocity. *Phys. Rev. D*, 101(5):056010, 2020.
- [124] B. Alessandro et al. psi-prime production in Pb-Pb collisions at 158-GeV/nucleon. *Eur. Phys. J. C*, 49:559–567, 2007.

- [125] Jaroslav Adam et al. Differential studies of inclusive J/ψ and $\psi(2S)$ production at forward rapidity in Pb-Pb collisions at $\sqrt{s_{NN}} = 2.76$ TeV. *JHEP*, 05:179, 2016.
- [126] Vardan Khachatryan et al. Measurement of Prompt $\psi(2S) \rightarrow J/\psi$ Yield Ratios in Pb-Pb and $p-p$ Collisions at $\sqrt{s_{NN}} = 2.76$ TeV. *Phys. Rev. Lett.*, 113(26):262301, 2014.
- [127] Albert M Sirunyan et al. Relative Modification of Prompt $\psi(2S)$ and J/ψ Yields from pp to PbPb Collisions at $\sqrt{s_{NN}} = 5.02$ TeV. *Phys. Rev. Lett.*, 118(16):162301, 2017.
- [128] Anton Andronic, Peter Braun-Munzinger, Krzysztof Redlich, and Johanna Stachel. Decoding the phase structure of QCD via particle production at high energy. *Nature*, 561(7723):321–330, 2018.
- [129] Axel Drees. Relative Yields and Nuclear Modification of ψ' to J/ψ mesons in p+p, p(^3He)+A Collisions at $\sqrt{s_{NN}} = 200$ GeV, measured in PHENIX. *Nucl. Part. Phys. Proc.*, 289-290:417–420, 2017.
- [130] Yannis Burnier, Olaf Kaczmarek, and Alexander Rothkopf. Quarkonium at finite temperature: Towards realistic phenomenology from first principles. *JHEP*, 12:101, 2015.
- [131] Yannis Burnier, Olaf Kaczmarek, and Alexander Rothkopf. Static quark-antiquark potential in the quark-gluon plasma from lattice QCD. *Phys. Rev. Lett.*, 114(8):082001, 2015.
- [132] A. Bazavov et al. Nonperturbative QCD Simulations with 2+1 Flavors of Improved Staggered Quarks. *Rev. Mod. Phys.*, 82:1349–1417, 2010.
- [133] Owe Philipsen. Constraining the QCD phase diagram at finite temperature and density. *PoS, LATTICE2019*:273, 2019.
- [134] Andrea Pelissetto and Ettore Vicari. Relevance of the axial anomaly at the finite-temperature chiral transition in QCD. *Phys. Rev. D*, 88(10):105018, 2013.
- [135] F Karsch, E Laermann, and Ch Schmidt. The Chiral critical point in three-flavor QCD. *Phys. Lett. B*, 520:41–49, 2001.
- [136] Philippe de Forcrand and Owe Philipsen. The QCD phase diagram for three degenerate flavors and small baryon density. *Nucl. Phys. B*, 673:170–186, 2003.
- [137] Xiao-Yong Jin, Yoshinobu Kuramashi, Yoshifumi Nakamura, Shinji Takeda, and Akira Ukawa. Critical endpoint of the finite temperature phase transition for three flavor QCD. *Phys. Rev. D*, 91(1):014508, 2015.
- [138] A. Bazavov, H. T. Ding, P. Hegde, F. Karsch, E. Laermann, Swagato Mukherjee, P. Petreczky, and C. Schmidt. Chiral phase structure of three flavor QCD at vanishing baryon number density. *Phys. Rev. D*, 95(7):074505, 2017.

- [139] Francesca Cuteri, Owe Philipsen, and Alessandro Sciarra. QCD chiral phase transition from noninteger numbers of flavors. *Phys. Rev. D*, 97(11):114511, 2018.
- [140] Owe Philipsen and Christopher Pinke. The $N_f = 2$ QCD chiral phase transition with Wilson fermions at zero and imaginary chemical potential. *Phys. Rev. D*, 93(11):114507, 2016.
- [141] David Anthony Clarke, Olaf Kaczmarek, Frithjof Karsch, Anirban Lahiri, and Mugdha Sarkar. Sensitivity of the Polyakov loop and related observables to chiral symmetry restoration. 8 2020.
- [142] H.T. Ding et al. Chiral Phase Transition Temperature in (2+1)-Flavor QCD. *Phys. Rev. Lett.*, 123(6):062002, 2019.
- [143] Heng-Tong Ding, Prasad Hegde, Olaf Kaczmarek, Frithjof Karsch, Anirban Lahiri, Sheng-Tai Li, Swagato Mukherjee, and Peter Petreczky. Chiral phase transition in (2 + 1)-flavor QCD. *PoS, LATTICE2018*:171, 2019.
- [144] H.-T. Ding, S.-T. Li, Swagato Mukherjee, A. Tomiya, X.-D. Wang, and Y. Zhang. Correlated Dirac eigenvalues and axial anomaly in chiral symmetric QCD. 10 2020.
- [145] Yoshinobu Kuramashi, Yoshifumi Nakamura, Hiroshi Ohno, and Shinji Takeda. Nature of the phase transition for finite temperature $N_f = 3$ QCD with nonperturbatively $O(a)$ improved Wilson fermions at $N_t = 12$. *Phys. Rev. D*, 101(5):054509, 2020.
- [146] Owe Philipsen and Christopher Pinke. Nature of the Roberge-Weiss transition in $N_f = 2$ QCD with Wilson fermions. *Phys. Rev. D*, 89(9):094504, 2014.
- [147] Philippe de Forcrand and Owe Philipsen. Constraining the QCD phase diagram by tricritical lines at imaginary chemical potential. *Phys. Rev. Lett.*, 105:152001, 2010.
- [148] Claudio Bonati, Guido Cossu, Massimo D’Elia, and Francesco Sanfilippo. The Roberge-Weiss endpoint in $N_f = 2$ QCD. *Phys. Rev. D*, 83:054505, 2011.
- [149] Philippe de Forcrand and Massimo D’Elia. Continuum limit and universality of the Columbia plot. *PoS, LATTICE2016*:081, 2017.
- [150] F. Karsch, E. Laermann, and A. Peikert. Quark mass and flavor dependence of the QCD phase transition. *Nucl. Phys. B*, 605:579–599, 2001.
- [151] Y. Iwasaki, K. Kanaya, S. Kaya, S. Sakai, and T. Yoshie. Finite temperature transitions in lattice QCD with Wilson quarks: Chiral transitions and the influence of the strange quark. *Phys. Rev. D*, 54:7010–7031, 1996.
- [152] Lukas Varnhorst. The $N_f=3$ critical endpoint with smeared staggered quarks. *PoS, LATTICE2014*:193, 2015.

- [153] Philippe de Forcrand, Seyong Kim, and Owe Philipsen. A QCD chiral critical point at small chemical potential: Is it there or not? *PoS*, LATTICE2007:178, 2007.
- [154] F. Karsch, C.R. Allton, S. Ejiri, S.J. Hands, O. Kaczmarek, E. Laermann, and C. Schmidt. Where is the chiral critical point in three flavor QCD? *Nucl. Phys. B Proc. Suppl.*, 129:614–616, 2004.
- [155] G. Endrodi, Z. Fodor, S.D. Katz, and K.K. Szabo. The Nature of the finite temperature QCD transition as a function of the quark masses. *PoS*, LATTICE2007:182, 2007.
- [156] H.-T. Ding, A. Bazavov, P. Hegde, F. Karsch, S. Mukherjee, and P. Petreczky. Exploring phase diagram of $N_f = 3$ QCD at $\mu = 0$ with HISQ fermions. *PoS*, LATTICE2011:191, 2011.
- [157] Francesca Cuteri, Owe Philipsen, Alena Schön, and Alessandro Sciarra. The deconfinement critical point of lattice QCD with $N_f = 2$ Wilson fermions. 9 2020.
- [158] Shinji Ejiri, Shota Itagaki, Ryo Iwami, Kazuyuki Kanaya, Masakiyo Kitazawa, Atsushi Kiyohara, Mizuki Shirogane, and Takashi Umeda. End point of the first-order phase transition of QCD in the heavy quark region by reweighting from quenched QCD. *Phys. Rev. D*, 101(5):054505, 2020.
- [159] Dmitri E. Kharzeev, Larry D. McLerran, and Harmen J. Warringa. The Effects of topological charge change in heavy ion collisions: 'Event by event P and CP violation'. *Nucl. Phys. A*, 803:227–253, 2008.
- [160] V. Skokov, A.Yu. Illarionov, and V. Toneev. Estimate of the magnetic field strength in heavy-ion collisions. *Int. J. Mod. Phys. A*, 24:5925–5932, 2009.
- [161] Wei-Tian Deng and Xu-Guang Huang. Event-by-event generation of electromagnetic fields in heavy-ion collisions. *Phys. Rev. C*, 85:044907, 2012.
- [162] Massimo D'Elia, Swagato Mukherjee, and Francesco Sanfilippo. QCD Phase Transition in a Strong Magnetic Background. *Phys. Rev. D*, 82:051501, 2010.
- [163] Igor A. Shovkovy. *Magnetic Catalysis: A Review*, volume 871, pages 13–49. 2013.
- [164] H.-T. Ding, S.-T. Li, A. Tomiya, X.-D. Wang, and Y. Zhang. Chiral properties of (2+1)-flavor QCD in strong magnetic fields at zero temperature. 8 2020.
- [165] Heng-Tong Ding, Christian Schmidt, Akio Tomiya, and Xiao-Dan Wang. Chiral phase structure of three flavor QCD in a background magnetic field. 6 2020.
- [166] G.S. Bali, F. Bruckmann, G. Endrodi, Z. Fodor, S.D. Katz, S. Krieg, A. Schafer, and K.K. Szabo. The QCD phase diagram for external magnetic fields. *JHEP*, 02:044, 2012.

- [167] G.S. Bali, F. Bruckmann, G. Endrodi, Z. Fodor, S.D. Katz, and A. Schafer. QCD quark condensate in external magnetic fields. *Phys. Rev. D*, 86:071502, 2012.
- [168] E. M. Ilgenfritz, M. Muller-Preussker, B. Petersson, and A. Schreiber. Magnetic catalysis (and inverse catalysis) at finite temperature in two-color lattice QCD. *Phys. Rev. D*, 89(5):054512, 2014.
- [169] V.G. Bornyakov, P.V. Buividovich, N. Cundy, O.A. Kochetkov, and A. Schäfer. Deconfinement transition in two-flavor lattice QCD with dynamical overlap fermions in an external magnetic field. *Phys. Rev. D*, 90(3):034501, 2014.
- [170] G.S. Bali, F. Bruckmann, G. Endrödi, S.D. Katz, and A. Schäfer. The QCD equation of state in background magnetic fields. *JHEP*, 08:177, 2014.
- [171] Akio Tomiya, Heng-Tong Ding, Xiao-Dan Wang, Yu Zhang, Swagato Mukherjee, and Christian Schmidt. Phase structure of three flavor QCD in external magnetic fields using HISQ fermions. *PoS, LATTICE2018*:163, 2019.
- [172] Massimo D’Elia and Francesco Negro. Chiral Properties of Strong Interactions in a Magnetic Background. *Phys. Rev. D*, 83:114028, 2011.
- [173] Jens O. Andersen, William R. Naylor, and Anders Tranberg. Phase diagram of QCD in a magnetic field: A review. *Rev. Mod. Phys.*, 88:025001, 2016.
- [174] Toru Kojo and Nan Su. The quark mass gap in a magnetic field. *Phys. Lett. B*, 720:192–197, 2013.
- [175] Falk Bruckmann, Gergely Endrodi, and Tamas G. Kovacs. Inverse magnetic catalysis and the Polyakov loop. *JHEP*, 04:112, 2013.
- [176] Kenji Fukushima and Yoshimasa Hidaka. Magnetic Catalysis Versus Magnetic Inhibition. *Phys. Rev. Lett.*, 110(3):031601, 2013.
- [177] M. Ferreira, P. Costa, O. Lourenço, T. Frederico, and C. Providência. Inverse magnetic catalysis in the (2+1)-flavor Nambu-Jona-Lasinio and Polyakov-Nambu-Jona-Lasinio models. *Phys. Rev. D*, 89(11):116011, 2014.
- [178] Lang Yu, Hao Liu, and Mei Huang. Spontaneous generation of local CP violation and inverse magnetic catalysis. *Phys. Rev. D*, 90(7):074009, 2014.
- [179] Bo Feng, Defu Hou, Hai-cang Ren, and Ping-ping Wu. Bose-Einstein Condensation of Bound Pairs of Relativistic Fermions in a Magnetic Field. *Phys. Rev. D*, 93(8):085019, 2016.
- [180] Xiang Li, Wei-Jie Fu, and Yu-Xin Liu. Thermodynamics of 2+1 Flavor Polyakov-Loop Quark-Meson Model under External Magnetic Field. *Phys. Rev. D*, 99(7):074029, 2019.

- [181] Shijun Mao. From inverse to delayed magnetic catalysis in a strong magnetic field. *Phys. Rev. D*, 94(3):036007, 2016.
- [182] Umut Gürsoy, Ioannis Iatrakis, Matti Järvinen, and Govert Nijs. Inverse Magnetic Catalysis from improved Holographic QCD in the Veneziano limit. *JHEP*, 03:053, 2017.
- [183] Kun Xu, Jingyi Chao, and Mei Huang. Spin polarization inducing diamagnetism, inverse magnetic catalysis and saturation behavior of charged pion spectra. 7 2020.
- [184] Massimo D’Elia, Floriano Manigrasso, Francesco Negro, and Francesco Sanfilippo. QCD phase diagram in a magnetic background for different values of the pion mass. *Phys. Rev. D*, 98(5):054509, 2018.
- [185] Gergely Endrodi, Matteo Giordano, Sandor D. Katz, T.G. Kovács, and Ferenc Pittler. Magnetic catalysis and inverse catalysis for heavy pions. *JHEP*, 07:007, 2019.
- [186] Claudio Bonati, Massimo D’Elia, Marco Mariti, Michele Mesiti, Francesco Negro, Andrea Rucci, and Francesco Sanfilippo. Magnetic field effects on the static quark potential at zero and finite temperature. *Phys. Rev. D*, 94(9):094007, 2016.
- [187] Murray Gell-Mann, R.J. Oakes, and B. Renner. Behavior of current divergences under $SU(3) \times SU(3)$. *Phys. Rev.*, 175:2195–2199, 1968.
- [188] J. Gasser and H. Leutwyler. Chiral Perturbation Theory: Expansions in the Mass of the Strange Quark. *Nucl. Phys. B*, 250:465–516, 1985.
- [189] Aftab Ahmad, Adnan Bashir, Marco A. Bedolla, and J.J. Cobos-Martínez. Color, Flavor, Temperature and Magnetic Field Dependence of QCD Phase Diagram: Magnetic Catalysis and its Inverse. 8 2020.
- [190] V.V. Braguta, M.N. Chernodub, A. Yu Kotov, A.V. Molochkov, and A.A. Nikolaev. Finite-density QCD transition in a magnetic background field. *Phys. Rev. D*, 100(11):114503, 2019.